# Protein supersaturation powers innate immune signaling

Alejandro Rodriguez Gama[1], Tayla Miller[1], Shriram Venkatesan[1], Jeffrey J. Lange[1], Jianzheng Wu[1], Xiaoqing Song[1], Dan Bradford[1], Jay R. Unruh[1], Randal Halfmann[1,2]

1. Stowers Institute for Medical Research, Kansas City, MO.
2. Department of Biochemistry and Molecular Biology, University of Kansas Medical Center, Kansas City, KS, USA

## Summary

Innate immunity protects us in youth but turns against us as we age. The reason for this tradeoff is unclear. Seeking a thermodynamic basis, we focused on death fold domains (DFDs), whose ordered polymerization has been stoichiometrically linked to innate immune signal amplification. We hypothesized that soluble ensembles of DFDs function as phase change batteries that store energy via supersaturation and subsequently release it through nucleated polymerization. Using imaging and FRET-based cytometry to characterize the phase behaviors of all 109 human DFDs, we found that the hubs of innate immune signaling networks encode large nucleation barriers that are intrinsically insulated from cross-pathway activation. We showed via optogenetics that supersaturation drives signal amplification and that the inflammasome is constitutively supersaturated *in vivo*. Our findings reveal that the soluble “inactive” states of adaptor DFDs function as essential, yet impermanent, kinetic barriers to inflammatory cell death, suggesting a thermodynamic driving force for aging.

# Introduction

Innate immune signaling transduces small signals to robust cellular responses. At the extremes, human cells respond to single molecules of pathogen origin with explosive inflammatory cell death.[1–7] This level of sensitivity and signal amplification is likely essential to defeat enemies that can otherwise rapidly self-replicate to catastrophic effect.

Signaling initiates when pathogen- or damage-associated molecular patterns (PAMPs or DAMPs) activate cognate receptor protein oligomers that then activate effector proteins such as transcriptional regulators and caspases, typically via one or more intermediary proteins known as adaptors. Most interactions between receptors, adaptors, and effectors involve death fold domains (DFDs), a large and ancient superfamily of homotypic interaction modules whose origin appears to have preceded eukaryotes.[8–11] DFDs comprise the caspase recruitment domain (CARD), death domain (DD), death effector domain (DED), and pyrin domain (PYD) subfamilies.

The energy released by tiny numbers of PAMPs or DAMPs binding to receptors is far too small to drive innate immune responses directly. The signal must be amplified in an energy consuming process.[12–14] Other signal transduction pathways achieve amplification by energizing signaling molecules using chemical fuel (e.g. ATP, GTP) or electrochemical gradients. In contrast, DFDs amplify signaling by forming stable open-ended polymers.[15–25] The polymers activate downstream signaling factors by simply localizing them to high proximity.[26,27] At sufficiently high concentrations in vitro or when overexpressed, some DFDs also template their own activation in a prion-like fashion without an overt energy source.[15–20,25] Whether they also do so at endogenous concentrations *in vivo* is not yet clear. Other DFDs fail to polymerize or do so without self-templating activity.[19,28–36] Therefore, despite consensus that DFD polymerization can provide a stoichiometric basis for signal amplification, the driving force for polymerization *in vivo* is not known.

Newly synthesized polypeptides lose free energy upon folding.[37,38] However, a few proteins can become stuck in metastable "native" states that retain some of this energy to drive a future change in activity when the protein is triggered by a stimulus to fold into its more stable conformation.[39,40] We posited that DFDs could also exist in inactive states that are metastable with respect to open-ended active polymers. The kinetic barrier for such a mechanism would be the initial formation, or nucleation, of the polymer. Nucleation occurs when a small number of protein subunits form an unstable embryo of the polymer that is just large enough to recruit more subunits.[41–43] The amount of energy required for the nucleus to form spontaneously, known as the nucleation barrier, is determined by the protein's supersaturation (concentration in excess of the polymer's solubility limit) and its sequence-encoded conformational preferences in the physiological environment. In extreme cases such as bona fide prions, the sequence-encoded component of the nucleation barrier (hereafter referred to as the "structural nucleation barrier") is so large in vivo that it preserves a deeply supersaturated state of the protein for years or decades before a nucleating event releases that energy.[44,45] Importantly, nucleation involves a tiny fraction of the available molecules of the protein and can occur without any external change to the proteins' folding landscape. This can allow for arbitrarily large numbers of

proteins to activate in response to vastly substoichiometric stimuli. We previously showed that life has exploited this property in at least one case: the DFD adaptor for the CBM signalosome, BCL10, uses this principle to activate pro-inflammatory NF-κB.[46] Owing to a sequence-encoded nucleation barrier, BCL10 is supersaturated even before stimulation and is therefore poised to respond decisively to fungal pathogen exposure. Is this a general paradigm for innate immune signaling, and if so, what advantage does it offer over classical signal transduction?

Effective signaling requires that a given signal be unequivocally linked to a specific response, while crosstalk between signaling pathways tends to be deleterious.[47,48] Prion-like proteins notoriously interact with other cellular factors to cause disease. How then could such a mechanism underlie innate immunity, where the consequence of even a single aberrant interaction leading to "unintended" nucleation could kill the cell? Alternatively, might some level of nucleating crosstalk functionally increase cells' robustness to pathogens?

These considerations lead us to hypothesize that DFDs function as phase change material in the biological equivalent of a thermal battery, wherein latent heat stored in a supersaturated phase is released on-demand by crystallization.[49,50] This energy source would play the role of e.g. ATP in other signaling cascades, with the important difference that the signal-amplifying DFD is precharged for the role. Our hypothesis makes the following predictions: 1) some DFDs of innate immune signaling will be able to populate cell-wide soluble states that are supersaturated with respect to assembled states; 2) structural ordering and thermodynamic stability of the assembled states will increase with the kinetic stability of the soluble states that precede them; 3) those DFDs will be constitutively supersaturated *in vivo* (i.e. prior to stimulation); and 4) at least some of the DFDs from different signaling pathways will supersaturate independently of each other. We here use a combination of biophysical, bioinformatic, and cytological approaches in both orthogonal nonhuman and physiological human cellular contexts to investigate the capacity for supersaturation-driven signal amplification by all human DFDs. Our results collectively support all four predictions and thereby uncover a thermodynamic driving force for innate immune signaling.

# Results

### Nucleation barriers are prevalent among DFDs

We previously reported that several DFDs whose activation accompanies ordered polymerization -- MAVS, ASC, and Bcl10 can supersaturate in cells [16,46]. Whether other DFDs share this property is central to our understanding of how innate immunity produces robust outputs from infinitesimal inputs. We used a sequence- and literature-guided search to identify 116 instances of DFDs in the human proteome, involving 104 human proteins (**Table S1 and Figure S1A**). Most of these are multidomain proteins with a single DFD at either terminus, a location that allows maximum accessibility for protein-protein interactions. Twelve proteins contained two DFDs, typically one closely following the other. To determine if the DFDs in such pairs should be evaluated separately or together, we used the Predicted Aligned Error (PAE) generated by AlphaFold.[51] PAE is the expected positional error at residue x if the predicted and actual structures are aligned on residue y. Seven of the DFD pairs exhibited very low

interdomain PAE scores comparable to those within the component DFDs (**Figure S1B,** bottom), suggesting a conserved fixed geometric relationship between the domains. We therefore considered these tandem DFDs as single members of their respective subfamilies, for a total of 109 DFD modules.

We sought to characterize the intrinsic phase behavior (sequence-encoded phase boundaries and kinetic barriers) of each DFD module, i.e. in the absence of other DFDs or regulatory interactions but under otherwise physiological conditions. For this purpose we used the budding yeast, *Saccharomyces cerevisiae*, as an orthogonal eukaryotic cell that completely lacks DFDs and their specific regulatory factors. We codon-optimized and cloned the DFDs for strong inducible expression as fusions to the bright and exceptionally monomeric amphifluorescent protein, mEos3.[52] The fusion was made opposite the native N- or C-terminus of each protein to minimize non-native steric effects.

We then used DAmFRET to analyze the self-association of each protein as a function of its accumulated intracellular concentration following twenty hours of expression. DAmFRET produces a snapshot of the population-level distribution of single-cell measurements of ratiometric FRET ("AmFRET") between the two fluorescent forms of mEos3. The data revealed a diversity of behaviors (**Figure 1A, 1B, S1C, and Table S1**), ranging from no self-association at any concentration to self-association in all cells at all concentrations. For many of the DFDs, cells formed both a low and a high AmFRET population with a continuous transition between the two populations. For 17 DFDs, the transition instead occurred discontinuously such that a range of DFD concentrations existed wherein cells with the same concentration populated either a low or high AmFRET value. These included the aforementioned DFDs of MAVS, ASC, and BCL10. We previously showed that discontinuous transitions result from large structural nucleation barriers that are characteristic of prion-like self-assembly.[43,46,53] We find this to be a surprisingly large number given the paucity of proteins with known prion-like behavior. For example, a systematic DAmFRET screen of the top 100 computationally predicted yeast prion-forming proteins found that only 14 exhibited discontinuous DAmFRET profiles.[54] We conclude that nucleation barriers are prevalent among DFDs.

Our hypothesis predicts that assemblies with structural nucleation barriers will tend to be more ordered and more stable than those lacking structural nucleation barriers. DFD polymerization can create microscopically visible filaments in cells.[18,46,55], whereas less-ordered assemblies tend to form spherical or amorphous puncta. To probe the relationship of structural nucleation barriers to ordered polymerization, we therefore examined the intracellular distribution of each DFD using high-throughput confocal microscopy. We found that all of the DFDs that populated AmFRET-positive states also formed visible assemblies, whereas only five of the 61 DFDs with entirely low AmFRET did so (**Figure 1A**). We further classified the assemblies as either fibrillar or punctate based on the aspect-ratios and coefficients of variation in cellular fluorescence (**Figure S1D**). Each of the DFD subfamilies exhibited a diversity of behaviors (**Figure 1B**). As predicted, however, the assemblies of DFDs that had transitioned discontinuously were almost invariably fibrillar (16 of 17, **Figure S1E, S1F and S1G**). So too were those of DFDs with continuous high DAmFRET (10 of 11). In contrast, only 8 of 19 DFDs with continuous low-to-high DAmFRET formed fibrillar assemblies; the rest were punctate. Hence, the microscopy data

confirm that discontinuous DAmFRET profiles of DFDs involve highly ordered polymerization, but not necessarily the other way round.

To next probe the relationship of structural nucleation barriers to polymer stability, we eliminated supersaturation to reveal each DFD's saturating concentration, which is determined by the strength of subunit interactions in its assembled structure. We did so by introducing artificial genetically-encoded "seeds" of each DFD. We designed these seeds to mimic the oligomerized states of full-length DFD proteins when they are naturally activated by PAMPs or DAMPs, by genetically fusing each DFD to an inert and well-characterized homomultimeric domain, μNS[56] (**Figure 1C**). We expected the resulting multimer to eliminate the nucleation barrier of the corresponding DFD expressed in trans, causing all cells with supersaturating concentrations of that DFD to switch from the low to the high AmFRET population[46] (**Figure 1D**). As expected, co-expressed self-seeds caused cells to switch to the high AmFRET population for most (12 of 17) discontinuous DFDs (**Figure 1E**). Analyzing two such examples by fluorescence microscopy, we observed a corona of filaments radiating outward from the μNS puncta (**Figure S1H,** bottom left and top right). To control for potential nonspecific effects of μNS-DFD fusions, we also expressed these two DFDs in the presence of each other's seed. Seeding did not occur in these cases (**Figure S1H**, top left and bottom right), confirming that it requires homotypic interactions between the seed and the corresponding DFD. Inspection of the DAmFRET plots of the five nonseedable discontinuous DFDs reveal that most are only slightly discontinuous. They include $CARD9^{CARD}$, which we previously showed to polymerize with a negligible nucleation barrier above its solubility limit of approximately 100 μM.[19] Hence, at least some of these five are false-positive in the unseeded analysis, presumably as a consequence of cell-to-cell heterogeneity in e.g. volume.[57] Most of the continuous DFDs (61 of 66) did not exhibit self-seeding **(Figure 1E, Table S1)**. As a proxy for saturating concentration, for each self-seeded DFD, we obtained the concentration at which half of cells exhibited AmFRET.[54] By comparing this value (EC50) to the corresponding values obtained in the absence of seed, we found that discontinuous DFDs achieved soluble concentrations that exceeded their saturating concentration by more than six-fold on average (**Figure 1F**). More importantly, and as predicted, discontinuous DFDs exhibited lower saturating concentrations than continuous DFDs (**Figure 1G, and Table S1**), confirming the expected relationship between structural nucleation barriers and polymer stability.

While our data thus far confirm that discontinuous DFDs undergo nucleation-limited self-assembly, it does not clarify if such assembly involves native DFD interactions rather than amyloid-like misfolding.[43] To answer that directly, we next introduced point mutations to disrupt assembly via conserved known interfaces between folded DFD subunits.[18,19] Across multiple DFDs examined, all such mutations indeed reduced or eliminated the high-AmFRET population (**Figure S2**). To more systematically evaluate the nature of DFD assembly in our experiments, we subjected the seeded and unseeded cells to semi-denaturing detergent-agarose gel electrophoresis (SDD-AGE), a technique that distinguishes amyloids from other protein states based on their detergent-resistance and size dispersity.[58] We found that unlike our amyloid control ($RIPK1^{RHIM}$), none of the DFD assemblies survived sarkosyl exposure (**Figure S1I**), consistent with their retaining the death fold rather than misfolding into amyloid. These data collectively suggest that multiple DFDs encode nucleation barriers large enough for them to accumulate to supersaturated levels while staying soluble over organismal timescales.

**Supersaturation is a defining feature of innate immune signaling hubs**

The depth of supersaturation *in vivo* is determined by the ratio of a protein's expression level to its saturating concentration.[59] Each term can evolve independently by gene regulation and DFD sequence, respectively. Consequently, if the function of discontinuous DFDs involves supersaturation, we can expect evolution to have increased their expression while decreasing their saturating concentrations, relative to those of continuous DFDs. Such a relationship would be unexpected in the absence of functional supersaturation, because most soluble proteins are only expressed to the edge of their saturating concentration.[60] Having already assessed saturating concentrations, we therefore next evaluated the expression level of each DFD in monocytes using published transcriptomic and proteomic datasets curated by the Protein Abundance Database and the Human Protein Atlas.[61,62] As predicted, discontinuous DFDs tended to have higher endogenous expression than continuous DFDs (**Figure 2A, S3A and Table S1**). This relationship persisted even in the whole body proteome (**Figure S3B**). We then asked how the saturating concentrations of DFDs relate to their expression levels in primary immune cells.[63] Remarkably transcript levels significantly anticorrelated with saturating concentrations in all 18 canonical immune cell populations (**Figure 2B and S3C**), confirming that discontinuous DFDs are likely to be supersaturated in their endogenous physiological contexts.

A protein's importance to a biological response can be approximated by its centrality in the corresponding network. Central proteins tend to be essential,[64] more abundant,[65] slower evolving,[66] and more frequently targeted by pathogens[65,67] than noncentral proteins. Proteins that have many direct interactions, or high "degree centrality", are hubs in protein-protein interaction networks. Proteins that bridge many other nodes, or have high "betweenness centrality", act as bottlenecks that disproportionately control information flow through the network. To gauge the importance of supersaturability to DFD signaling pathways, we therefore assessed these two fundamental centrality measures for all DFD-containing proteins in the network of physically interacting DFD-containing proteins, as extracted from the STRING database.[68] Proteins with discontinuous and/or seedable DFDs proved to have greater degree and betweenness centralities than those with continuous or non-seedable DFDs (**Figure 2C and S3D**), consistent with greater control by the former over pathway activity and an essential executive function of supersaturation in innate immunity.

For a DFD nucleation barrier to function as hypothesized, the DFD must be supersaturated (soluble yet poised for polymerization) in the context of its full-length (FL) protein. Any interactions with other parts of the protein that either lower the nucleation barrier or increase thermodynamic solubility would reduce the extent of supersaturation and therefore capacity to drive signal amplification. Multiple DFDs that are otherwise capable of polymerization are prevented from doing so by autoinhibitory interactions in the context of full-length protein oligomers.[19,31–36] Our screen of isolated DFDs already included five FL proteins that consist of little more than the DFD itself; none of these were supersaturable. We therefore evaluated the phase behaviors of 21 diverse DFD-containing FL multidomain proteins. Many of the proteins behaved comparably to their corresponding DFDs (**Figure 2D, Figure S4A, and Table S2**). Others had continuous low or moderate DAmFRET even though their isolated DFDs had

polymerized discontinuously to high AmFRET, consistent with autoinhibited oligomerization. We confirmed this interpretation for one of these (NLRP3) by showing that seeds of the DFD, but not the FL protein itself, eliminated the nucleation barrier of its cognate adaptor (ASC; see below and **Figure S4B**). Five of the FL proteins were, however, comparably or even more supersaturable than their corresponding DFDs. These collectively represent all four DFD subfamilies: BCL10 and MAVS (driven by CARD), TRADD (driven by DD), FADD (driven by DED), and ASC (driven by PYD and CARD). Strikingly, all of these function specifically as adaptors in well-characterized signalosomes of innate immunity, where they link multiple PAMP or DAMP receptors to one or more effectors (**Figure 2E**). In contrast, signalosomes that are less specific to innate immunity, particularly the apoptosome, the PIDDosome, and the EDA receptor complex, lacked supersaturation (**Figure 2F**). These data reveal that interactions of the DFD with the surrounding protein context can either inhibit or enhance supersaturation, but that the latter occurs preferentially (if not exclusively) among adaptors with innate immune signaling functions. That these prion-like adaptor proteins are the hubs of their respective signaling networks agrees with their hypothesized executive function.

**Supersaturation drives signal amplification in human cells**

We next asked if supersaturation drives signal amplification *in vivo*. We focused on the intrinsic pathway of apoptosis, by which cell death normally occurs in response to persistent intracellular stresses.[69–71] Consistent with the relatively muted signaling of this pathway relative to, for example, pyroptosis, we found that the apoptosome lacks supersaturable DFDs (**Figure S5A**).

To test if the absence of nucleation barriers contributes to noncommittal signaling through the apoptosome, we adapted an optogenetic approach that exploits the reversible oligomerization of Cry2clust in response to 488 nm blue light[26,46,72] to allow for precise experimental control over apoptosome initiation. HEK293T cells lack the inflammasome constituents NLRC4, ASC, and CASP1, allowing us to repurpose their DFDs in this cell line. Accordingly, we transduced the cells with mScarlet fusions of either the non-supersaturable WT apoptosome effector, CASP9, or a chimeric version that harbored the supersaturable DFD of CASP1 in place of its own ($CASP9^{CASP1CARD}$). We simultaneously transduced the cells with blue light-inducible seeds of the cognate upstream DFD -- opto-APAF1 or opto-NLRC4, respectively (**Figure 3A**). Cry2clust oligomerizes within seconds after stimulation and then reverts back to its monomeric form over several minutes.[72,73] Therefore, to first compare the abilities of the reconstituted apoptosomes to transmit signals irrespective of amplification, we measured the activation of CASP3/7, the downstream target of CASP9, after just one minute of blue light stimulation. We found that both cell lines activated a fluorescent CASP3/7 reporter to the same extent at this timepoint (**Figure 3B**), revealing that the WT and chimeric protein pairs comparably activate CASP9 while they are oligomerized.

To now assess DFD-mediated signal amplification, we evaluated both the persistence of DFD assemblies and their ability to commit cells to apoptosis following an otherwise sublethal stimulus. We anticipated that cells expressing the non supersaturated pair of apoptosome proteins will 1) form reversible clusters and consequently 2) survive a short blue light stimulus. In contrast, cells expressing the supersaturated pair of proteins will 1) form irreversible clusters

that prolong signaling, and consequently 2) die even after a short blue light stimulus. To test prediction 1, we stimulated the cells with blue light for one minute and monitored subsequent protein localization. We found that both proteins coalesced to visible puncta in essentially all cells within 15 minutes. Both of the CASP9 variants followed suit (**Figure 3C,D**). The WT puncta then dissolved over the course of the next ten minutes. In contrast, the chimeric puncta instead continued to grow at a constant rate for at least the next 40 minutes (**Figure 3C,D**), as expected.

To test prediction 2, we measured cell death two hours after the initiation of blue light stimulation for either one minute or the full two hours. Neither the WT nor chimeric pair of proteins induced cell death in the absence of blue light, as determined by an absence of cells staining with Annexin V (**Figure 3E**). The WT protein pair induced death in approximately 18% and 55% of cells following the short and long stimulation, respectively (**Figure 3E**), confirming the expected dose-dependence of signaling. The chimeric protein pair induced death in most cells even for the short stimulation, revealing that supersaturation amplified signaling to a greater extent than had been achieved by the non-supersaturated native DFDs of intrinsic apoptosis.

**Innate immune cell death is driven by endogenously supersaturated adaptors**

We next asked if supersaturation functions in innate immunity at endogenous expression levels, by focusing on extrinsic apoptosis and pyroptosis in human THP-1 monocytes. We first treated the monocytes with poly(dA:dT), a ligand for the inflammasome receptor, AIM2. By 18 hours, approximately 70% of the cells were dead or dying, as determined by double positive staining with Sytox and Annexin V-Alexa-488. We then deleted *PYCARD* to determine if cell death depended on ASC, the adaptor for the inflammasome and pyroptosis. Death was delayed, but not eliminated (**Figure 4A**). Crosstalk has been observed between the inflammasome and extrinsic apoptosis signaling.[74–79] We therefore also deleted *FADD*, the adaptor for extrinsic apoptosis, and found that death was reduced further still (**Figure 4A and S5B**). These data reveal that AIM2 activation triggers programmed cell death through both ASC and FADD.

To eliminate the potentially confounding activation of orthogonal dsDNA sensors,[80] we fused $AIM2^{PYD}$ to the miRFP670nano fluorescent protein followed by Cry2clust (**Figure 4B**). We found that when expressed in HEK293T cells -- which lack the downstream effectors of AIM2 that would otherwise kill the cells upon stimulation -- the protein rapidly and persistently clustered following a 10-second blue laser pulse. We next introduced the F27G mutation to disrupt a critical PYD-PYD interface.[18] In contrast to WT, the mutant protein clusters dissociated within 15 minutes following the blue light pulse (**Figure 4C**), altogether confirming that this fusion protein -- hereafter dubbed “opto-AIM2” -- grants direct control over $AIM2^{PYD}$ seed formation.

We therefore proceeded to express opto-AIM2 in THP-1 cells. We subjected the cells to 1 second of 488 nm laser excitation every 15 minutes while monitoring cell death through CellTox incorporation. This regime sufficed to kill essentially all cells within one hour (**Figure 4D**). In the absence of ASC (*PYCARD*-KO), approximately 50% of cells still died, but now with delayed kinetics consistent with the known hierarchical activation of apoptosis when pyroptosis fails [81–83]. Cell death was completely eliminated by the F27G mutation, irrespective of the presence of

ASC, confirming that both modes of cell death involve AIM2 making canonical DFD polymer interactions.

We reasoned that if ASC and/or FADD are supersaturated, a pulse of blue light will suffice to kill the cells. As expected, we found that a 10-second blue laser pulse triggered persistent protein clustering and cell death within six minutes, as indicated by Sytox Orange accumulation in the cytoplasm and nucleus (**Figure 4E**). Persistent clustering and cell death were both eliminated by the F27G mutation, confirming their dependence on PYD-PYD interactions (**Figure 4E**).

We next directly investigated inflammasome assembly in response to blue light by reconstituting the *PYCARD*-KO with doxycycline-inducible ASC. To allow us to monitor ASC expression level and localization in live cells, we fused to its C-terminus mScarlet-I, a rapidly maturing and fully monomeric fluorescent protein.[84,85], and expressed the protein to a lower level than endogenous ASC (**Figure S5C-D**) to ensure that it is not aberrantly supersaturated. We then tracked $AIM2^{PYD}$ and ASC localization following a 10-second blue laser pulse. Both proteins began to cluster almost immediately. $AIM2^{PYD}$ clusters then ceased growing by 10 minutes, whereas ASC clusters continued to grow for the full duration of the half hour time course (**Figure 4F**), confirming that a strong thermodynamic drive for ASC self-assembly exists even in the absence of stimulus.

ASC polymers serve as a platform for CASP1 molecules to activate themselves by self-cleavage in trans. Activated CASP1 then causes pyroptosis by activating gasdermin D (GSDMD) to form pores in the plasma membrane.[86] We therefore also assessed membrane integrity via CellTox incorporation either before the pulse or 30 minutes after, a timepoint that coincides with the cessation of CASP1 activity and full GSDMD cleavage.[87] The pulse indeed induced membrane permeabilization (**Figure 4G**). The efficiency of ASC clustering (**Figure 4F**) and the fraction of cells staining with CellTox (those above the dashed line in **Figure 4G**) did not depend on its expression level even when reduced to 10% that of endogenous (**Figure S5C-E**). These data, along with the specificity of our stimulus and the rapidity of the response, lead us to conclude that endogenous ASC exists in a deeply supersaturated state prior to stimulation.

Multiple mechanisms beyond ASC polymerization can in principle amplify signaling via the inflammasome. Nevertheless, we observed that the intensity of CellTox staining at the cellular level increased with ASC expression across the range tested (**Figure 4G**). Given the low (~50 nM) saturating concentration for ASC polymers,[88] this observation suggests a stoichiometric dependence of signal amplification on polymerized ASC subunits.

**The nucleating interactome is highly specific**

The evolution of signaling networks is limited by crosstalk between pathways.[47,48] Given that DFDs all share the same fold and are co-expressed in many of the same cells, they should be highly susceptible to nucleating each other. This would be functional when it occurs between DFDs in the same pathway, but likely deleterious when it occurs between DFDs in different pathways. To determine specificity and systematically map the nucleating interactome of DFDs, we mated our library of seed-expressing yeast strains with a library of strains expressing each

mEos3-fused DFD (**Figure S6A**) to create over 10,000 arrayed diploid yeast strains that we then systematically screened by DAmFRET (**Figure S6B and C**).

In total, we identified 171 nucleating interactions, representing just ~1.5% of the total library. These were consistently detected and highly reproducible in replicate experiments (**Figure S6D-F and Table S4**). Most of the interactions were homotypic (within the same subfamily; **Figure 5A and B**) and recapitulated known signaling relationships, such as DDX58 activating MAVS in the antiviral MAVS signalosome;[17] CARD9 activating BCL10 in the antifungal CBM signalosome;[19] and NLRP3 activating ASC and in turn CASP1 in the inflammasome.[18] Moreover, nucleating interactions were largely constrained to members of the same signaling subnetwork. For example, CARDs of the CBM signalosome nucleated each other but not CARDs of the inflammasome, and vice versa. We nevertheless did observe a small amount of crosstalk, most notably between the PYDs of the inflammasome and the DEDs of the Death-Inducing Signaling Complex (DISC) (**Figure 5C**). These nucleating interactions, for example between $AIM2^{PYD}$ and $CASP8^{2DED}$, are consistent with the close phylogenetic relationship between PYDs and DEDs,[89] and may be responsible for the residual cell death in *ASC FADD* double knockout cells shown in Figure 4A. They are consistent with known endogenous crosstalk between pyroptosis and extrinsic apoptosis signaling that is critical for defense against certain pathogens.[76,78,82]

On the whole, the observed network of nucleating interactions confirm that DFDs from different pathways are generally independently supersaturable. The supersaturable DFDs are nevertheless hardwired via structurally-encoded nucleating interactions to specific autorepressed signal receptors and effectors, consistent with their soluble ensembles functioning to power innate immune signal amplification.

# Discussion

DFDs polymerize to transduce innate immune signals across the tree of life,[22–24] but the energetics of how they do so had not been studied systematically. We investigated the possibility that soluble DFD ensembles store energy for signal amplification. We tested that hypothesis by comparing the supersaturabilities of all human DFDs in a tractable model of their physiological context, revealing that 17 of the 109 DFD modules exhibit nucleation barriers sufficient for them to globally supersaturate living cells. These nucleation barriers occurred preferentially in the hub of the DFD-containing protein interaction network, whereby they exert maximum control over information flow. We examined one such node in its endogenous context and confirmed it to be constitutively supersaturated. Whereas the vast majority of soluble proteins are expressed only to their respective thermodynamic solubility limits,[60] DFDs exhibit the opposite trend, highlighting the functional relevance of their supersaturation.

Our findings challenge the implicit assumption that ASC and other signalosome adaptors are thermodynamically inhibited prior to stimulation.[1,90] Instead, given that their soluble expression levels likely far exceed their saturating concentrations for active polymerization, kinetic barriers

are the principal determinant of their activity. For a typical cell, the absence of a structural template appears to be the only thing preventing it from self-destructing at any moment.

**DFDs are phase change batteries**

Our data altogether establish that adaptor DFDs of innate immunity are the biological equivalent of thermal batteries, wherein latent heat stored in a supersaturated "phase change material" is released by crystallization.[49,50] The larger the structural nucleation barrier, the more supersaturated the material can be and the greater and more stable the charge stored by the battery. Since the structural nucleation barrier is dominated by the entropic cost of soluble subunits forming a nucleus that is, itself, soluble,[41,42] the phase change material in innate immune batteries -- that is, soluble DFD ensembles -- will have evolved by natural selection *against* mutants that assemble too readily, as doing so would lower the nucleation barrier and therefore capacity of the battery. Once the nucleus forms, either spontaneously or through interactions with PAMPs or DAMPs, the battery discharges to drive amplification through near-crystalline polymerization.

We found that each of the major signalosomes has approximately one such battery. Some prominent innate immune signaling pathways appear to diverge from this trend, however. Most notable is the adaptor for the Myddosome, MYD88, which links the activation of Toll-like receptors (TLRs) to DFD-containing effector proteins,[91] and which did not supersaturate in our experiments **(Figure S4A)**. Our finding is consistent with the finite oligomeric structure of the Myddosome,[91,92]. The hypothetical battery of the Myddosome may lie upstream of MYD88. In particular, the non-DFD-containing adaptor protein, MAL, is typically required for Myddosome assembly[93–97] and has been shown to form self-assembling filaments *in vitro*[98] via its Toll/Interleukin-1 Receptor (TIR) domain. Alternatively, MYD88 may be a false negative in our experiments, perhaps as a consequence of the fact that, unlike other adaptors which transition from monomer to polymer, MYD88 activation involves a transition between different multimeric states[92,99] that may not be discernibly different by DAmFRET. MYD88 was previously found to exhibit a nucleation barrier *in vitro*[100,101] and to form switch-like and persistent assemblies at the subcellular level in vivo.[99] Further study will be required to determine if MYD88 and/or MAL are supersaturated in vivo.

The other DFD-containing pathways that lacked structural nucleation barriers also lack strong connections to pathogen defense, specifically the intrinsic apoptosome, the PIDDosome, and the EDA pathway for ectoderm differentiation. We note that unlike the pathways with supersaturable adaptors, which execute life-or-death decisions informed by minute signals of pathogen infection, these pathways function in tissue homeostasis and differentiation informed by persistent sterile host-derived signals.[102,103] Hence, our systematic comparison of all human DFDs identifies structural nucleation barriers specifically in pathogen defense pathways, consistent with the extraordinary degree of signal amplification necessitated by this function. We suspect that the battery-like function of DFDs is ancestral because pyroptosis-like defensive cell death appears to have preceded apoptosis and even the emergence of eukaryotes.[77]

## Implications for structure-function relationships

The functions that dictate DFD structure are presumed to emerge from the material polymers, and specifically, their unbounded stoichiometry.[22–24] However, the polymers' functions appear not to constrain DFD structure, based on the fact that arbitrarily condensing or even dimerizing innate immune effector proteins suffices to transduce signaling,[26,27,46]. This suggests that the specifics of DFD polymer structure are dispensable for effector activation. In contrast, the battery-like function of supersaturated DFDs does constrain polymer structure. The constraint is indirect. Because battery capacity increases with the near-inability of soluble "inactive" ensembles to activate, the structure of the "active" state necessarily becomes more ordered. This is a consequence of evolution eliminating soluble conformers that too readily self-associate, leaving only an ensemble that fails to self-assemble spontaneously despite a thermodynamic drive to do so. Interactions between subunits correspondingly strengthen to offset the entropic cost of polymerization.[41] This perspective explains why strictly linear polymers, such as by DIX and SAM domains, are not employed in innate immunity despite their abundance in other signaling pathways.[104] Relative to these polymers that are structurally less restrictive but fundamentally lack a nucleation barrier, DFDs polymerize through two-dimensional crystallization,[27] which creates a tunable nucleation barrier. That this feature rather than other properties of DFDs explains their use in innate immunity is supported by the fact that innate immune signaling pathways have evolved from at least two other unrelated protein domains that likewise polymerize in effectively two-dimensions: TIR domains and amyloids, the latter of which are in most other contexts dysfunctional.[22,27]

## Functional logic of phase change batteries in immunity

Most signal transduction cascades use chemical fuel or electrochemical gradients to amplify signaling in the form of high-energy or otherwise short-lived states.[12–14,105] Examples include phosphorylated proteins that are rapidly dephosphorylated, high local concentrations of molecules that diffuse away, ions that are rapidly pumped back across the membrane, or caspase heterodimers that irreversibly dissociate. These pathways are consequently "off" at steady state. Allowing the pathways to reset provides for more dynamic signaling that is also more forgiving of aberrant activation. By contrast, adaptor DFD polymerization represents the equilibration of an already high energy system. Notwithstanding negative feedback mechanisms such as autophagy[106] that can rid the cell of the polymers in some circumstances, the polymerized "on" state is effectively irreversible. Indeed, the polymers can outlive the cell of origin and propagate inflammation when taken up by other cells.[15]

Why should innate immunity use this unusual and unforgiving mode of signal amplification? The most obvious explanation is that innate immune signaling is often terminal -- the cells differentiate or die, by necessity to protect the organism. Another reason may be that crystallization processes are inherently specific. The extraordinary specificity revealed in our cross-seeding analysis shows that despite their overtly similar structures, each supersaturated DFD stockpiles energy that is privately accessible only to itself, its immediate partners, and no other proteins in the cell. This not only allows each pathway to operate independently, it

insulates them from other cellular processes and metabolic fluctuations that could aberrantly activate the pathway to immediately lethal consequence.[47,48,107]

Enzyme folds are evolutionarily constrained by the fixed properties of their substrate. By comparison, and despite their high specificity for self, protein self-assembles have few structural constraints. Amyloid formation is a “default” capability of polypeptides,[108] and symmetric homo-oligomers tend to be susceptible to polymerization.[109] It is therefore possible that the inexhaustible sequence space that can support structural nucleation barriers benefits the host in the never-ending evolutionary arms race against pathogens.

Phase change batteries discharge in response to nucleating stimuli. The relative lability of receptor polymers (**Table S1**) and their tendency to be autoinhibited by non DFDs agrees with current interpretations that they function as nuclei for adaptor DFD polymers when uninhibited by binding to PAMPs or DAMPs.[22–24] Consistent with this role and the frequently multivalent nature of PAMPs and DAMPs, condensing DFDs in the absence of autoinhibitory non-DFD interactions generally eliminated barriers to polymer nucleation. That the multimeric nature of DFD polymers may heighten the sensitivity of signaling to PAMPs and DAMPs through cooperative effects is well-appreciated.[22–24] Nevertheless, cooperativity is limited by the small sizes of the polymers’ nuclei,[21,110] and is therefore insufficient to explain the use of polymers over finite oligomers.

A cooperativity function also fails to explain the use of polymerization over disordered condensation, which offers unlimited cooperativity near phase boundaries for liquid-liquid phase separation (LLPS).[111] DFD-mediated polymerization has comparably limited ability to distinguish small differences in PAMP/DAMP concentration or valency. However, the absence of a structural nucleation barrier means that the susceptibility of LLPS to spontaneous nucleation increases dramatically beyond its phase boundary (**Figure 6A**).[41,43] DFD proteins are therefore unlikely to be endogenously supersaturated with respect to LLPS, and their activation via this mechanism will be stoichiometrically limited by the concentration and valency of the respective PAMP/DAMP. In short, LLPS offers sensitivity but not signal amplification. However, coupling receptor LLPS to adaptor nucleation may allow pathways to maximize both sensitivity and amplification. Consistent with this possibility, some receptor proteins have recently been found to undergo LLPS via co-condensation of their non-DFDs with PAMPs/DAMPs.[112,113] Whether receptor LLPS will prove to be the rule or the exception remains to be determined.

### Implications for aging

Hyperactive innate immune signaling is a causal hallmark of aging.[114] Our findings suggest a simple thermodynamic basis for that relationship. The absence of a structural template appears to be the only thing that prevents self-destruction at any moment of a cell’s life. Every supersaturated protein creates an eventuality that will befall the cell if it lives long enough, whether that fate is nucleated by the intended signal or instead by an unintended but ultimately inevitable molecular fluctuation. Might DFD supersaturation therefore limit cell lifespan? As a prelude to answering that question in future work, we extended the analysis in Fig. 2B and S3C to all human cell types, and simply asked how DFD supersaturation (as approximated by the anticorrelation between DFD EC50 and expression level) relates to the mean lifespan of each

cell type in the human body.[115] From this we see that short-lived cells such as granulocytes and endothelial cells indeed appear to be more deeply supersaturated than long-lived cells such as oocytes and neurons (**Figure 6B and S7**).

We suspect that innate immune signaling networks have evolved to minimize the vulnerability to spontaneous self-destruction by functionalizing a minimal set of supersaturated adaptors through an expanding cadre of non-supersaturable receptors, effectors, and regulators. It is for this reason, we believe, that despite a fundamental role of self-assembly in collective DFD function, only a small fraction of human DFDs proved to be supersaturable. The extent to which those supersaturated DFDs limit longevity at both the cellular and organismal levels is now an essential question for further study.

**Limitations of the study**

Multiple DFDs were found to populate stable ordered polymers in all cells. Although we did not observe a nucleation barrier for these, it is possible that they could still be supersaturable in vivo at much lower than the micromolar concentrations surveyed by DAmFRET. Similarly, a small number of DFDs that populated only a low AmFRET state did not express to high concentrations in yeast, and it is possible that they can self-assemble under cellular contexts that allow them to reach higher concentrations.

Our study necessarily simplifies and abstracts human innate immune signaling. We considered the cytoplasm of living yeast cells to be a suitable proxy for the physiological context of DFDs *as a whole*, but the exact context of endogenous DFDs will differ from that in our experiments. For example, several of the DFDs normally localize to the nucleus in human cells, and this could impact their phase behavior. Note, however, that none of these exhibited a structural nucleation barrier in our experiments, suggesting that if anything our findings may underreport the number of DFD batteries. Similarly, our work does not consider the roles of transcriptional regulation and post-translational modifications (PTMs). For example, NLRP3 is upregulated and becomes phosphorylated in response to LPS “priming” of the inflammasome,[116] and polyubiquitination of RIG-I promotes its activation of MAVS.[117] Such modifications imply that some signal amplification occurs upstream of supersaturated adaptors. Whether or to what extent each adaptor is supersaturated will differ between cell types and biological contexts, as a consequence of regulated expression, post-translational modifications, and binding partners. Such regulation will change how much of the corresponding battery’s capacity is used in that context.

# Materials and Methods

**Key Resources Table**

| Reagent type (species) or resource | Designation | Source or reference | Identifiers | Additional information |
|---|---|---|---|---|
| *S. cerevisiae*, strain background: S288c | rhy1713 | PMID: 29979963 | | |
| *S. cerevisiae*, strain background: S288c | rhy2153 | PMID: 35727133 | | |
| *S. cerevisiae*, strain background: S288c | rhy2977 | PMID: 36920097 | | |
| Cell line (*H. sapiens*) | HEK293T | American Type Culture Collection | # CRL-3216 | |
| Cell line (*H. sapiens*) | THP-1 | American Type Culture Collection | # TIB-202 | |
| Cell line (*H. sapiens*) | THP-1 PYCARD-KO | Invivogen | thp-koascz | |
| antibody | anti-Actin | Santa Cruz Biotechnology | sc-8432 | Protein Simple (1:50); Western Blot (1:1000) |
| antibody | anti-PYCARD | Santa Cruz Biotechnology | sc-514414 | Protein Simple (1:200); Western Blot (1:1000) |
| antibody | anti-FADD | Sigma-Aldrich | 05-486 | Protein Simple (1:10); Western Blot (1:500) |

| | | | | |
|---|---|---|---|---|
| recombinant DNA reagent | pCW57.1-PYCARD-mScarlet | This paper | | Lentiviral plasmid for expressing HsPYCARD-(4xEAAAR)-mScarlet-I from an inducible Doxycicline promoter |
| recombinant DNA reagent | pLV_AIM2-PYD-miRFP670-Cry2clust | This paper | | Lentiviral plasmid for expressing HsAIM2(PYD)-(4xEAAAR)-miRFP670nano-Cry2clust from a constitutive promoter |
| commercial assay or kit | Sytox Orange | ThermoFisher | S11368 | 1:1000 |
| commercial assay or kit | Annexin V Alexa568 | ThermoFisher | A13202 | 1:200 |
| commercial assay or kit | Annexin V Alexa488 | ThermoFisher | A13201 | 1:200 |
| commercial assay or kit | Incucyte® Caspase-3/7 Dye | Sartorius | 4440 | 1:1000 |
| software, algorithm | Fiji/ImageJ | http://fiji.sc | RRID:SCR_002285 | |
| software, algorithm | GraphPad Prism 9 | https://www.graphpad.com/ | RRID:SCR_002798 | |

**Reagents and antibodies**

Hygromycin B (Invivogen, ant-hg-1), Penicillin-Streptomycin (ThermoFisher, 1514014gp), PMA (BioVision, 1544-5), Puromycin (Invivogen, ant-pr-1), Sytox Orange (ThermoFisher, S11368), CellTox (Promega, G8741), Annexin V Alexa568 (ThermoFisher, A13202), Annexin V Alexa488 (ThermoFisher, A13201), Incucyte® Caspase-3/7 Dye (Sartorius, 4440). Antibodies, anti-ASC

(Santa Cruz Biotechnology, sc-514414), anti-FADD (Sigma, 05-486), anti-Actin (Santa Cruz Biotechnology, sc-8432) were obtained from the indicated vendors.

**Plasmid construction**

Yeast expression plasmids were made as previously described[43]. Briefly, we used a golden gate cloning-compatible high copy episomal vector, V08, which contains inverted BsaI sites followed by a rigid helical linker 4x(EAAAR) and mEos3.1. This vector drives the expression of proteins from a *GAL1* promoter and contains the auxotrophic marker *URA3*. The vector V12 is identical to V08 except that mEos3.1 and linker precedes rather than follows the BsaI sites, for expressing proteins with an N-terminal fusion. Inserts were ordered as GeneArt Strings (Thermo Fisher) flanked by Type IIs restriction sites for ligation between BsaI sites in V08 and V12. All other inserts were cloned into respective vectors via Gibson assembly between the promoter and respective tag. All plasmids were verified by Sanger sequencing. All expression plasmids are listed in **Table S1**.

Lentivirus vectors were as previously described[46]. Briefly, optogenetic constructs were cloned into pLV-EF1a-IRES-Hygro (Addgene #85134) which encodes a Hygromycin B resistance cassette. To create lentiviral vectors expressing the the optogenetic constructs fused with miRFP670nano and Cry2, the corresponding sequences of AIM2$^{PYD}$, APAF1$^{CARD}$, NLRC4$^{CARD}$ were inserted via Gibson assembly into pLV-EF1a-IRES-Hygro. Finally, The doxycycline-controlled lentiviral vectors were cloned via Gibson assembly with the respective coding sequences from PYCARD, CASP9, CASP1, and mScarlet-I into pCW57.1 (Addgene #41393). All lentivirus vectors are listed in **Table S3**.

**Yeast strain construction**

Unseeded DAmFRET experiments were conducted using strain rhy1713.[43] To create strains expressing DFD seeds, we first transformed AseI digests of each DFD plasmid along with a plasmid expressing Cas9 and a guideRNA targeting the *URA3* markers into rhy2153. This strain contains a genomic landing pad consisting of natMX followed by the *tetO7* promoter and counterselectable *URA3* ORFs derived from *C. albicans* and *K. lactis*, and stop-µNS-mCardinal as described[46]. Successful integration of the insert replaces the *URA3* marker with the gene of interest and fuses to the protein's C-terminus µNS-mCardinal, under the control of a doxycycline-repressible promoter. Transformants were selected for resistance to 5-FOA and validated for successful seed integration by detection of mCardinal expression using flow cytometry. The arrayed library of resulting strains was then mated to each of the rhy1713 strains expressing separate DFD-mEos3.1 fusions, by pinning each pair of strains together onto agar omnitrays containing SD-URA+NAT+Dox media. The resulting colonies were then pinned into liquid SD-URA+NAT+Dox for continued diploid selection and creation of glycerol stocks. The entire nucleating interaction screening consisted of 384 96-well plates.

**DAmFRET assay preparation and data collection**

We performed DAmFRET as previously described.[43] Briefly, single transformant yeast colonies were inoculated in 200 µl of SD-URA in a 96-well microplate well and incubated in a Heidolph

Titramax platform shaker at 30°C, 1350 RPM overnight. Cells were washed with sterile water, resuspended in galactose-containing media, and allowed to continue incubating for approximately 20 hours. Microplates were then illuminated for 25 min with 320–500 nm violet light to photoconvert a fraction of mEos3 molecules from a green (516 nm) form to a red form (581 nm). At this point, cells were either used to collect microscopy data or continue the DAmFRET protocol.

For the nucleating interaction screen, glycerol stock plates were pinned into liquid SD-URA without dox and incubated for 16 hours at 30°C with 1350 RPM shaking overnight. We then resuspended cells in fresh SD-URA media and continued incubation for an additional 20 hours. After this, we resuspended cells in SGal-URA and continued incubation for 20 hours to induce protein expression. Finally, we resuspended cells in fresh SGal-URA for four hours prior to DAmFRET data collection. The library was then consolidated into 96 384-well plates.

DAmFRET data were collected on a ZE5 cell analyzer cytometer. Autofluorescence was detected with 405 nm excitation and 460/22 nm emission; SSC and FSC were detected with 488 nm excitation and 488/10 nm emission. Donor and FRET fluorescence were detected with 488 nm excitation and 425/35 nm or 593/52 nm emission, respectively. Acceptor fluorescence was detected with 561 nm excitation and 589/15 nm emission. For each well, we collected a volume of 13 µL, resulting in approximately 500,000 events per sample. Data compensation was done in the built-in tool for compensation (Everest software V1.1) on single-color controls: non-photoconverted mEos3.1 and dsRed2 (as a proxy for the red form of mEos3). For nucleating interactions, we included an additional channel for mCardinal intensity with 561 nm excitation and 670/30 nm emission.

**DAmFRET data analysis**

Data were processed on FCS Express Plus 6.04.0015 software (De Novo). Events were gated for single unbudded cells by FSC vs. SSC, followed by gating of live cells with low autofluorescence and positive donor and acceptor fluorescence. With the exception of TNFRSF10A$^{DD}$ (TRAIL-R1) (rhx2933) which failed to express with either its C- or N-terminus tagged, all expression plasmids were processed. Plots represent the distribution of AmFRET (FRET intensity/acceptor intensity) vs. Acceptor intensity (protein expression).

We then analyzed the data as previously described.[53] Briefly, FCS files were gated using an automated R-script running in flowCore. Before gating, the forward scatter (FS00.A, FS00.W, FS00.H), side scatter (SS02.A), donor fluorescence (FL03.A), and autofluorescence (FL17.A) channels were transformed using a logicle transform in R. Single cells were gated using FS00.A vs SS02.A and FS00.H vs FS00.W. These were gated for expressing cells using FL03.A vs FL17.A. Cells falling within these gates were then exported as FCS3.0 files for further analysis.

DAmFRET histograms were divided into 64 logarithmically spaced bins across a predetermined range large enough to accommodate all data sets. The upper gate values were determined for each bin as the 99th percentile of the DAmFRET distribution in that bin. We used the expression of mEos3.1 alone to delineate the region of a DAmFRET plot that corresponds to no assembly. For all samples, cells falling above this region are considered to contain protein assemblies

(FRET-positive). The fraction of cells in the assembled population was plotted as a ratio to the total cells in the bin for all 64 bins. The gross fraction of such cells expressing a given protein is reported as fgate.

**Determination of continuity**

We initially attempted to classify each DAmFRET dataset as one-state or two-state, and discontinuous or continuous for the latter, using an algorithm previously developed for this purpose.[54] However, the algorithm invariably misclassified discontinuous datasets as "continuous" when the AmFRET level of the high FRET state changed with concentration, i.e. exhibited positive or negative slope as for $FAS^{DD}$ and $CASP2^{CARD}$, respectively. Due to this limitation, we adopted a different method.

To determine the continuity of an adequately expressed plasmid, we analyzed the distribution of the AmFRET values about the transition point. To do so, we fit a spline to the median AmFRET values across binned concentrations ranging from the 1st to 99th percentile of concentration values. The starting point of the spline was determined as the first bin with at least 1000 cells that reached at least the 20th percentile of all bin densities, as measured by the number of events divided by the interquartile range (IQR) of AmFRET values within the bin. The number of bins was determined using the Freedman-Diaconis rule. The median AmFRET values were calculated for each bin, and then denoised using the python scipy.signal package, resulting in the spline fit. The transition point was then defined as the maximum of the first derivative of the fitted spline, using the numpy.diff package. We then used Hartigan & Hartigan's dip test for unimodality to determine the continuity on a narrow window of +/- 12% of the expression range around the transition point. The width of the window was chosen to account for the variability in and guided by the distribution of concentration values across the transition point of robustly self-seeded samples. We classified each plot as "discontinuous" or "continuous" for p values less than or greater than 0.05, respectively. The latter were further classified by KMeans clustering into three categories, wherein AmFRET values were either uniformly low ("low"), uniformly high ("high"), or transitioned from low to high with increasing concentration ("low to high"). We derived clustering parameters from the spline fit, encompassing overall change, maximum consecutive change, minimum, and end AmFRET values, along with the fraction of positive AmFRET. We transformed the fraction positive AmFRET data into log10 and also calculated the cube root of the ending AmFRET values. We standardized all parameters, giving twice the weight to the fraction positive, minimum, and ending AmFRET values compared to other parameters.

**Calculating centrality measures**

To determine betweenness and degree of centrality, we extracted interactions involving DFD-containing proteins (listed in **Table S1**) from STRING version 12.0, considering only physical interactions with scores of 900 or higher. Using NetworkX v3.1, we analyzed these interactions as an undirected graph to calculate betweenness and degree of centrality. For proteins with multiple DFDs, we classified a protein as discontinuous if any of its DFDs were identified as discontinuous.

**Determination of positive nucleating interactions**

We first excluded files with fewer than 2500 events positive for mEos3 or mean acceptor intensities less than 3.5 AU. From this, any DFD or seed left with less than 25% of their original instances after filtering were removed from the analysis completely. Next, we identified nucleating interactions as DFD pairs that decreased the EC50 and increased the fraction assembled (fgate). We standardized all variables for each experimental batch of DFDs to a mean of 0 and variance of 1. We then determined the outlier degree for EC50 and fgate based on the number of interquartile ranges below or above the median for these values. This was done directionally on a per-DFD basis. We defined the “nucleating interactions” for a given mEos3-fused DFD as those whose mean of these two values (reported as “seedability”) is greater than or equal to 3 standard deviations above the mean of all seedability values. We confirmed that the seedability values for most DFD pairs partitioned with that of two negative controls included for each DFD.

To evaluate the reproducibility of our assay, we replicated it for a set of 36 DFDs. This replicate analysis mirrored the original, except it utilized the DFD distributions and cutoff values from the first set. The Pearson correlation (R) between the two sets was 0.91 ($p < 0.0001$). To minimize the impact of random variations in negatives and outliers, we excluded double negative instances, resulting in a slightly altered Pearson correlation (R) of 0.90 ($p < 0.0001$). Of the 3478 DFD + seed combinations reassessed, 17 showed inconsistent hit-calling, indicating an assay consistency rate of 99.51% with a 95% confidence interval ranging from 99.28% to 99.74%.

**Approximating saturating concentrations**

To generate an average DAmFRET curve, we computed the mean of each histogram bin in the DAmFRET dataset, focusing on bins containing a minimum of 100 cells. The average DAmFRET curve for each DFD in the presence of its self-seed was fit to a Weibull function as follows. We first calculated the average AmFRET value in each concentration bin. The resulting curves resemble the fraction-assembled curves except that the asymptote is the maximum AmFRET value rather than 1. Therefore, we used the following equation for fitting:

$$\square\square\square\square\square\square\square(\square) = \square\square\square[1 - \square\square\square(-\square\square(2)(\frac{\square}{\square\square 50})^{\square})] \quad \text{(Eq. 1)}$$

Here Amp is the AmFRET asymptotic value of the curve, c is the concentration, EC50 is the concentration at which the curve has reached 50% of its asymptotic value, and $\square$ is related to the steepness of the stretched exponential. Initial values of the parameters were chosen based on Gaussian smoothed versions of the curves and constrained in the fit to at minimum a 2-fold change from those initial guesses. The $\square$ parameter was constrained between 0.1 and 10 based on expected reasonable values of that parameter. At low and high concentration values, the average AmFRET values are clearly unstable and influenced by noise and minor compensation errors. Therefore, we chose the beginning and ending points of each curve by visual inspection, choosing starting points where the curve begins to increase and ending points

where the curve levels off. Error values were determined from Monte Carlo simulations as in the fitting of fraction assembly.

### Approximating supersaturability

To approximate the supersaturability of DFDs, the average EC50 of seeds that were deemed to have a nucleating interaction were compared to the average of those that did not, for each DFD, as a ratio. Only EC50s from accurate Weibull fits were used for this analysis, as determined by their requiring 10 or fewer iterations for the function to be fit. The median fold change reduction for discontinuous DFDs was found to be 6.0078, with a range of 3.6010 to 14.0324. The fold change reduction in EC50 for discontinuous DFDs was compared to continuous DFDs and found to be significantly higher. Mann Whitney U=1.0 (p=0.0004), $n_{continuous} = 9$, $n_{discontinuous} = 10$. The continuous DFDs that exhibited positive seeding interactions were either fibrillar or diffuse, not punctate as characterized in Figure 1A, when imaged in the absence of seeding. This suggests that they likely form ordered polymers, much like the discontinuous DFD counterparts.

### Cell culture

HEK293T cells and THP-1 cells were purchased from ATCC. THP-1 *PYCARD*-KO (thp-koascz) cells were purchased from InvivoGen. HEK293T cells were grown in Dulbecco's Modified Eagle's Medium (DMEM) with L-glutamine, 10% fetal bovine serum (FBS), and PenStrep 100U/mL. THP-1 cells were grown in Roswell Park Memorial Institute (RPMI) medium 1640 with L-glutamine and 10% FBS. All cells were grown at 37°C in a 5% CO2 atmosphere incubator. Cell lines were regularly tested for mycoplasma using the Universal mycoplasma detection kit (ATCC, #30-1012K).

### Generation of stable cell lines

Stable cell lines were created as described.[46] Briefly, constructs were packaged into lentivirus in a 10 cm plate 60% confluent of HEK293T cells using the TransIT-LT1 (Mirus Bio, MIR2300) transfection reagent and 7 µg of the vector, 7 µg psPAX2, and 1 µg pVSV-G. Lentivirus was harvested and incubated with 293T with polybrene or infected at 1000x g for 1 hour for THP-1 cells. For transduction of pCW57.1 derived vectors, HEK293T and THP-1 cells were selected with Puromycin (1 µg/mL) for 7 days. After this time, cells were sorted for positive expression of mScarlet and expanded in continuing selection with puromycin. For transduction of plasmids encoding fusions to miRFP670nano-Cryclust, THP-1 and HEK293T cells were selected with Hygromycin B (350 µg/mL and 150 µg/ml, respectively) for 7 days. Cells were sorted for positive expression of miRFP670nano and expanded for further experiments with continued selection. To generate THP-1 PYCARD-KO + FADD-KO cells, sgRNA targeting FADD exon1 was cloned into the lentiCRISPR v2-Blast (Addgene #83480). This vector was packaged into lentivirus as described above. THP-1 PYCARD-KO cells were transduced using spinfection and supplemented with polybrene. 24 hr after spinfection, media was replaced. 48 hr after spinfection, cells were selected with blasticidin (1 µg/ml). After 10 days of blasticidin selection, single-cell clonal expansion was done by serial dilution of resistant cells to achieve complete knockouts. Selected wells were analyzed by immunoblot to confirm the absence of FADD protein and sequence-verified.

### High-content imaging analysis

High-content imaging was performed on the Opera Phenix high-content screening system (PerkinElmer) using a 63x water immersion objective. Briefly, yeast (rhy2977) transformed with individual plasmids were cultured and induced as for DAmFRET assays. Then, 10 µl were transferred into a well containing 90 µl of SGal-URA of a 96-well optically clear flat-bottom plate (PerkinElmer 6055302). Data analysis of the high content imaging was performed in Fiji. Images of mEos3 were acquired using 488 nm excitation and a standard GFP filter set. Small z stacks were acquired over 5 µm total range with 1 µm steps. The image containing the brightest mEos3 signal was used. The mEos3 signal was then background-subtracted with a rolling ball radius of 100 pixels then found and converted to Fiji ROIs using the Fiji Default method of traditional image thresholding. The mean, standard deviation, and aspect ratio (AR) were measured for each object. The coefficient of variation (CV) in pixel intensity was calculated for every object following the formula: CV = Std Dev/Mean*100. The wells were divided into 3 categories based on their AR and CV. Objects that had a CV > 55 and an AR > 1.159 were designated “fibrillar”. Objects that had a CV > 55 and an AR < 1.16 were designated “punctate”. Finally, objects that had a CV < 55 and an AR < 1.16 were designated “diffuse”. These cutoffs were determined manually from a visual inspection of the data. The results were then manually verified for all wells. We found inconsistent classification by these cutoffs for plasmids (rhx2935, rhx2637, rhx0989) due to heterogeneity in the structures formed. We also detected three DFDs with anomalously high AR (rhx1113, rhx1097, rhx2937) due to their low expression. Plasmids rhx4763 - rhx4767 were acquired in a second data set that used different laser powers and integration times. Hence, for these plasmids specifically, “fibrillar” had a CV > 17 and an AR > 1.4, “punctate” had a CV > 17 and an AR < 1.41, and “diffuse” had a CV < 18 and an AR < 1.41. These cutoffs were determined manually from a visual inspection of the data. The results were then manually verified for several wells.

### Fluorescence microscopy and optogenetic activation

The yeast and mammalian cells were imaged in an LSM 780 microscope with a 63x Plan-Apochromat (NA = 1.40) objective. T-Sapphire was excited with a 405 nm laser. mEos3 and mScarlet-I were excited with a 488 nm and 561 nm laser, respectively. For time-lapse imaging, samples were maintained at 37 °C and 5% CO2 with a stage top incubator. To stimulate Cry2clust we used the 488 nm laser at a power setting of 50% for a pulse of 10 seconds, which is the amount of time it took to scan the user-generated region of interest unless indicated otherwise. 561 and 633 nm lasers were used for imaging mScarlet-I and miRFP670nano, respectively. Pyroptosis events were tracked by incorporating the Sytox Orange reagent into the cell. To quantify the CV, images were subjected to an in-house Fiji adapted implementation of Cellpose[118] for cellular segmentation. The Cellpose-generated regions of interest (ROIs) were used to measure specified imaging channels.

For quantification of cell dead events using IncuCyte (Sartorius), THP-1 cells were plated on a 24 or 96 well plate at a density of $4x10^8$/well or $1x10^8$/well, respectively, with PMA (10 ng/mL) for 16 hrs. Media was replaced with fresh media supplemented with Annexin V-Alexa488 and Sytox Orange. For AIM2-Cry2clust activation, an initial collection of unexposed measurements

was taken for 30 min. Then, the plate was exposed to 488 nm laser every 5 min. For treatments with poly(dA:dT), cells were treated and immediately subjected to imaging every 30 minutes for 19 hours. Positive cells for either fluorophore were indentified using the integrated software in the IncuCyte instrument.

For optogenetic activation of APAF1$^{CARD}$ and NCLR4$^{CARD}$, HEK293T cells expressing lentivirus constructs were seeded on a 35-mm dish (ibidi) at a density of $4x10^4$/mL with 2 mL of media. The next day, Dox was added at a concentration of 1 µg/mL to induce the expression of mScarlet tagged proteins. Twenty-four hours after protein induction, media was replaced with fresh media supplemented with Incucyte® Caspase-3/7 Dye (4440) 2 hours prior to the experiment or Annexin V-Alexa488. Cells were imaged using a spinning-disk confocal microscope (Nikon, CSU-W1) with a ×60 Plan Apochromat objective (NA = 1.40) and a Flash 4 sCMOS camera (Hamamatsu). A region of interest (ROI) was selected to induce optogenetic activation for indicated times using a 488 nm laser at 50% laser power for the indicated time ranging from a fraction of a second to 30 seconds. ROIs were generated by Cellpose segmentation algorithm around each cell contour. These ROIs were then used to measure the area, mean, standard deviation, and integrated density of each cell on the 488 nm and 560 nm fluorescence channels.

**Protein immunodetection**

We performed capillary based protein immunodetection (Wes, Simple Protein) as described.[46] Briefly, protein lysates were prepared as per recommended manufacturer instructions to a final concentration of 1 µg/ml. An assay plate was filled with samples, blocking reagent, primary antibodies (1:50 dilution for anti-Actin, 1:200 dilution for anti PYCARD), HRP-conjugated secondary antibodies and chemiluminescent substrate. The plate was subjected to electrophoretic protein separation and immunodetection in the fully automated capillary system. The rulting data was processed using the open-source software Compass (https://www.proteinsimple.com/compass/downloads/) to extract the intensities for the peaks corresponding to the expected molecular weight of proteins of interest. For Western Blot, cells were centrifuged at 1000 x g for 5 min and resuspended in lysis buffer (50 mM Tris (pH 7.4), 137 mM NaCl, 1 mM EDTA, 1% Triton X-100, 10 mM DTT (dithiothreitol), cOmplete protease inhibitor (1 tablet / 10 ml) (Roche, 11697498001). Protein lysates were resolved on a NuPAGE™ 4 to 12%, Bis-Tris gel and transferred onto a PVDF membrane (IPVH00010, Millipore) using the Pierce Power Blotter (ThermoFisher). The membrane was blocked with 5% skim milk and incubated overnight with the antibodies: anti-Actin (1:1000, sc-8432), anti-FADD (1:500, 05-486) and anti-PYCARD (1:1000, sc-514414). Primary antibody was removed by several washes with TBS + 0.1% Tween-20 and then subjected to incubation with secondary antibody (anti-mouse-HRP, 7076S, Cell Signaling Technology). The detection of protein bands was then carried out using enhanced chemiluminescence (ECL) (SuperSignal West Pico Chemiluminescent Substrate, ThermoFisher, 34577). The chemiluminescent signal was acquired by placing the membrane in a film cassette and exposing it to X-ray film (Kodak) at varying durations in a darkroom. After exposure, films were developed using an automatic film processor.

### Semi-Denaturating Detergent Agarose Gel Electrophoresis (SDD-AGE)

SDD-AGE was performed as previously described.[43] Briefly, cells were lysed using a 2010 Geno/Grinder with bead-beating. Samples were prepared with 2% sarkosyl and separated in a 1.5% agarose gel with 0.1% SDS. The distribution of mEos3-fused proteins was analyzed directly in the gel with a GE Typhoon Imaging System. Images were processed to remove background using a 250-pixel rolling ball, cropped, and contrast-adjusted.

### Quantification and statistical analysis

Two-sided Student's t-tests were used for significance testing unless stated otherwise for two sample comparisons. The graphs represent the means ± SEM of independent biological experiments unless stated otherwise. Statistical analysis was performed using GraphPad Prism 9, Python and R packages.

# Figure legends

Figure 1. **Nucleation barriers are prevalent among DFDs**

A. Illustration showing how the concentration-dependence of self-assembly as classified by DAmFRET (left) relates to the subcellular morphology of self-assemblies classified by high-throughput confocal microscopy (right). The number of DFDs in each link are indicated.
B. Distribution of DAmFRET classifications across the four subfamilies of DFDs.
C. Schematic of our experimental design to assess the ability of each DFD to seed itself. Top: Biological activation of the exemplary signalosome -- the Aim2 inflammasome -- occurs when the receptor Aim2 oligomerizes on the multivalent PAMP, dsDNA, and then templates the polymerization of the adaptor protein, ASC. Bottom: Experimental activation of potentially supersaturated DFDs was designed to mimic biological activation, by expressing each DFD in trans with the same DFD expressed as a fusion to the modular condensate-forming protein, μNS.
D. Representative DAmFRET data contrasting a supersaturable protein (left) with one that is not supersaturable (right). Note that the supersaturated protein exhibits a discontinuous distribution of AmFRET across the expression range. The dashed horizontal line approximates the mean AmFRET value for monomeric mEos3. Procedure Defined Units (p.d.u).
E. Heat map of seedability values showing that DFDs that have discontinuous DAmFRET classifications tend to be seedable. Procedure Defined Units (p.d.u).
F. Degree of supersaturability represented as the fold change reduction in EC50. Discontinuous DFDs show a significantly higher reduction in the EC50 when compared to continuous DFDs. Mann Whitney U=1.0 (p=0.0004), $n_{continuous}$ = 9, $n_{discontinuous}$ = 10. See Degree of supersaturability under Materials and Methods, for details.

G. Boxplot comparing the EC50 values of continuous and discontinuous DFDs when seeded. Discontinuous DFDs have significantly lower EC50 values, indicating greater polymer stability. Mann Whitney U = 179, $n_{continuous}$ = 17, $n_{discontinuous}$ = 13 (p = 0.0006).

See also Figures S1, S2, and Table S1.

Figure 2. **Supersaturation is a defining feature of innate immune signaling hubs**

A. Boxplot comparing the endogenous expression levels of continuous and discontinuous DFD-containing proteins indicating discontinuous DFDs have higher protein abundances in monocytes. Mann Whitney U = 40, $n_{continuous}$ = 27, $n_{discontinuous}$ = 8 (p = 0.0385). Protein Abundance values are from PAXdb.[61]
B. Scatter plot of Monocyte normalized Transcript per Million and EC50 values for self-seeded DFDs. Spearman R = -0.271 (p = 0.03). Adaptor DFDs are highlighted. Dataset extracted from Human Protein Atlas
C. Top, box plots of degree centrality and betweenness centrality of discontinuous and continuous DFDs in the endogenous network of physically interacting DFD proteins, revealing that the former are more centrally positioned in the network. For both centrality measures $n_{continuous}$ = 50, $n_{discontinuous}$ = 14. For degree centrality, Mann Whitney U = 190.5 (p = 0.0093). For betweenness centrality, Mann Whitney U = 188.5 (p = 0.0063). Bottom, box plots of centrality measures of non-seedable and seedable DFDs as determined in Figure 1E. For both centrality measures $n_{non\text{-}seedable}$ = 35, $n_{seedable}$ = 16. For degree centrality, Mann Whitney U = 167.5 (p = 0.0219). For betweenness centrality, Mann Whitney U = 172.5 (p = 0.0227).
D. Visualization of how the DAmFRET profiles of isolated DFD domains (left) change in their full-length contexts (right), showing that only adaptor proteins (green connections) tend to retain discontinuous transitions in their full-length context.
E. Subnetworks of prominent signalosome adaptor proteins that were found to be supersaturable. Edges connect nodes with experimentally determined physical interactions with confidence > 0.9 in STRING. All proteins shown have DFDs except TRAFs.
F. Subnetworks of signalosomes lacking supersaturable DFDs. Edges connect nodes with experimentally determined physical interactions with confidence > 0.9 in STRING. All proteins shown have DFDs except TRAF6.

See also Figures S3 and S4, and Tables S1 and S2.

Figure 3. **Supersaturation drives signal amplification in human cells**

A. Schematic of experiment in HEK293T cells to reconstitute the apoptosome with optogenetic control, in either a nonsupersaturable or supersaturable format. The nonsupersaturable format comprises the typical $APAF1^{CARD}$ and CASP9 pair; the supersaturable format comprises the chimeric APAF1 with $NLRC4^{CARD}$ in place of $APAF1^{CARD}$ and chimeric CASP9 with $CASP1^{CARD}$ replacing $CASP9^{CARD}$ ($CASP9^{CASP1CARD}$).
B. Caspase 3/7 activity reporter fluorescence intensities in the absence of stimulation or after 1 min 488 nm stimulation for cell lines expressing the nonsupersaturable or

supersaturable pairs, showing that both pairs signal comparably to CASP3 while oligomerized. P-value derived from Mann-Whitney analysis. APAF1$^{CARD}$-Cry2 + CASP9-mScarlet, Dark n = 163, Pulse n = 375. NLRC4$^{CARD}$-Cry2 + CASP9$^{CASP1CARD}$, Dark n = 46, Pulse n = 305.

C. Coefficient of variation (CV) of fluorescence distribution in HEK293T cells expressing the indicated protein pairs after a single 1 minute 488 nm laser activation. Top, APAF1$^{CARD}$-Cry2 and CASP9-mScarlet display rapid cluster formation that dissociates by 20 min. Bottom, NLRC4$^{CARD}$-Cry2 and chimeric CASP9$^{CASP1CARD}$ cluster less rapidly but the clusters continue to grow indefinitely.

D. Representative images from experiment in C. Clusters of APAF1$^{CARD}$-Cry2 and CASP9-mScarlet form then dissociate while NLRC4$^{CARD}$-Cry2 and CASP9$^{CASP1CARD}$ crusters only get larger.

E. Quantification of cell death of the HEK293T chimeric cells (as in A) using Annexin V-Alexa 488 staining, either two hours after a single 1 minute pulse of 488 nm laser, or after two hours of “constant” stimulation whereby cells were subjected to a 1 second pulse every 1 min. p-value derived from t-test.

See also Figure S5 and Table S3.

Figure 4. **Innate immune cell death is driven by endogenously supersaturated adaptors**

A. Time course of apoptotic cell death of THP-1 cells following exposure to AIM2 ligand, poly(dA:dT). p-value obtained from ANOVA followed by pair comparison.

B. Schematic of the experiment to transiently optogenetically stimulate AIM2$^{PYD}$ to monitor the dynamics of ASC$^{PYD}$ assembly. This experiment was conducted in HEK293T cells because they do not undergo pyroptosis.

C. Time course of fluorescence intensity distribution in HEK293T cells following 10 seconds of optogenetic activation, showing that WT AIM2$^{PYD}$ forms clusters (high CV) that persist, while the F27G mutant forms clusters that subsequently disperse.

D. Time course of cell death of THP-1 cells when subjected to a blue light pulse every 5 minutes (“repeated”), showing rapid cell death (violet trace) only when AIM2$^{PYD}$ is WT and when ASC is present. The absence of ASC results in slower death (green trace), consistent with apoptosis. The F27G mutation of AIM2$^{PYD}$ blocks cell death irrespective of ASC (black and golden traces).

E. Representative confocal microscopy images from a timelapse of individual THP-1 monocytes showing that transient optogenetic stimulation of WT but not F27G mutant of AIM2$^{PYD}$ causes it to form puncta that coincide with cell death. Sytox Orange was used for this experiment because it can be excited without activating Cry2.

F. Coefficient of variation (CV) of fluorescence distribution of AIM2$^{PYD}$-Cry2 and ASC-mScarlet in THP-1 *PYCARD-KO* cells following a 10s blue light pulse. This shows that AIM2$^{PYD}$ and ASC-mScarlet (with slightly delayed kinetics) rapidly form clusters that persist well after stimulus removal. ASC-mScarlet was induced to only ~20% of the ASC expression in WT cells using 1.0 µg/ml Doxycycline (Dox).

G. Quantification of CellTox staining in individual ASC-mScarlet THP-1 *PYCARD-KO* cells 30 minutes after a 10 second blue laser pulse, at different levels of Dox-induced ASC-mScarlet expression. Green dotted line indicates 95 % confidence interval (CI) for

background fluorescence intensity, above which cells were considered CellTox-positive. Error bars denote standard deviation. Control, n = 37. 0.25 µg/mL Dox, n = 36. 0.5 µg/mL Dox, n = 47. 0.75 µg/mL Dox, n = 113. 1 µg/mL Dox, n = 180.

See also Figure S5 and Table S3.

Figure 5. **The nucleating interactome is highly specific**

A. Matrix of all nucleating interactions (gray-shaded circles) detected in a comprehensive DAmFRET screen of > 10,000 DFD pairs. Each DFD-mEos3 (columns) was separately expressed with each DFD-µNS seed (rows). Darker shading of the circle denotes increased seedability. Interactions among members of the same signaling pathway (in legend) appear in color shaded squares. Asterisk denotes seeds that were screened in a separate experiment from the rest. The matrix was clustered on seedability values, on a log scale, using the scipy.cluster.hierarchy v1.11.1 linkage and dendrogram Python packages, using the Ward variance minimization algorithm to calculate distances. Procedure Defined Units (p.d.u).
B. Circos plot of the nucleating interactions summarized by DFD subfamily. Each subfamily is represented with a segment proportional to the number of DFDs with a nucleating interaction, as indicated by ribbons within and between segments. Inner stacked bars around the perimeter show the numbers of DFDs in each subfamily seeded by the subfamily in that segment. Middle stacked bars around the perimeter show the numbers of DFDs in each subfamily that seed the subfamily in that segment. Outer stacked bars around the perimeter show total nucleating interactions involving the subfamily in that segment.
C. Nucleating interactions involving DFDs in extrinsic apoptosis and pyroptosis, with blue edges highlighting the direct nucleating effect of AIM2 on FADD and ASC that is explored in Figure 4. The network was created in Cytoscape with node size corresponding to betweenness centrality and grouped by reported function. Interactions between full length proteins (Table S2) were included. Edge darkness indicates the seedability score of the corresponding interaction.

See also Figure S6 and Table S4

Figure 6. **Structural nucleation barriers allow DFDs to act as phase change batteries**

A. Top: Nucleation barrier as a function of protein concentration. The nucleation barrier for phase separation is highest at the saturating concentration ($C_{sat}$). For phase separation in the absence of structural ordering (LLPS, yellow solid line), the nucleation barrier declines precipitously with concentration above $C_{sat}$. While this allows LLPS to respond to small changes in PAMP/DAMP concentrations or valencies that lower $C_{sat}$ (red arrowhead), it prevents the system from achieving deep supersaturation. For phase separation concomitant with structural ordering (DFD polymer, blue solid line), the nucleation barrier falls more gradually with concentration above $C_{sat}$, allowing the system to achieve deep supersaturation (dashed blue line). The energy released by PAMP or DAMP binding to a receptor protein complex can trigger nucleation (dashed red line). Bottom: Following nucleation, the polymers grow and deplete soluble protein until it is no longer supersaturated (solid red arrow). Hence the extent of supersaturation at the time

of nucleation determines the extent to which the nucleating signal can be amplified. The structural nucleation barrier encoded by the soluble DFD ensemble therefore acts as a battery to power innate immune signal amplification.

B. Scatter plot of the anticorrelation between DFD transcription level and EC50 versus mean lifespan for each cell type in the human body.[115] Cell types with a significant anticorrelation, suggesting increased DFD supersaturation, have shorter lifespans than cell types without an anticorrelation.

# Supplementary figure legends

Figure S1. **Sequence, imaging and DAmFRET analysis reveal diverse sequence-encoded phase behaviors of DFDs, related to Figure 1**

A. Schematic of all DFDs characterized in this paper, and their classification into structural subfamilies. Tandem DFDs are highlighted in red, but were analyzed with their corresponding single DFD subfamilies.
B. Matrices of Predicted Alignment Error (PAE) for the indicated regions of proteins containing two DFDs, as reported in the AlphaFold Protein Structure Database,[51] grouped into two categories according to interdomain PAE values consistent with either independent (left) or dependent (right) relative geometries of the DFDs.
C. DAmFRET profiles of representative DFDs classified as continuous or discontinuous.
D. Classification of the proteins as entirely diffuse, fibrillar or punctate based on boundaries on the scatter plot of coefficient of variation vs aspect ratio. The colored circles represent the mean and covariance of the values for each category.
E. Analysis showing a prominence of fibrillar morphology of DFDs that had a discontinuous DAmFRET profile (chi-square contingency test, $p<0.001$).
F. Images of yeast expressing representative DFDs classified as fibrillar that produced continuous (low to high) DAmFRET profiles.
G. Images of yeast expressing representative DFDs classified as fibrillar that produced discontinuous DAmFRET profiles.
H. Representative confocal microscopy images of yeast expressing the indicated DFD constructs in the presence of the ASC or $CARD14^{CARD}$ seeds. The images show the emergence of filaments from homotypic but not heterotypic μNS-DFD seeds.
I. Image of SDD-AGE showing the size distribution of detergent-resistant multimers (where present) of mEos3-fused proteins expressed in yeast. The amyloid-forming protein, $RIPK1^{RHIM}$, formed detergent-resistant multimers whereas all DFD multimers were detergent-labile.

Figure S2. **Self-assembly involves subunit interfaces shared with solved DFD polymer structures, related to Figure 1**

Representative DAmFRET plots for the indicated DFDs with the indicated point mutations. The horizontal line approximates the mean AmFRET value for monomeric mEos3. Procedure Defined Units (p.d.u).

Figure S3. **Proteins with DFDs that have seedable and/or discontinuous DAmFRET are central to their physical interaction networks and are more likely to be supersaturated *in vivo*, related to Figure 2**

A. Transcripts encoding proteins with discontinuous DFDs have higher expression (normalized Transcipts Per Million, nTPM) in monocytes. Mann Whitney U = 378, $n_{continuous} = 84$, $n_{discontinuous} = 15$ ($p = 0.0137$). nTPM values were extracted from the single cell RNA dataset from the Human Protein Atlas.

B. Proteins with discontinuous DFDs have higher protein abundances at the whole organism level. Mann Whitney U = 400.5, $n_{continuous}$ = 82, $n_{discontinuous}$ = 16 (p = 0.0295).
C. Bar plot of the Spearman R correlation between immune cell type transcript abundance and EC50 values of DFDs shows consistent negative and significant anticorrelation among immune cell types. Transcript data was obtained from the immune cell section of the Human Protein Atlas.
D. Boxplot comparing the betweenness (left) and degree centrality (right) of DFD-containing proteins that are either non-seedable or continuous (n = 53) to those that are both seedable and discontinuous (n = 16). Seedable, discontinuous proteins were found to have a significantly higher betweenness and degree centrality than non-seedable or continuous proteins. Mann Whitney U = 134 (p = 0.0035) and U = 160.5 (p = 0.0192), respectively.

Figure S4. **Proteins characterized as signaling adaptors display discontinuity in its DFD and FL context, related to Figure 2**

A. Pairs of DAmFRET plots comparing the behaviors of representative DFDs and their corresponding full-length proteins. Dashed horizontal lines approximate the mean AmFRET value for monomeric mEos3. FL MAVS has appreciable AmFRET in the supersaturated state due to its mitochondrial localization signal that sequesters it to internal membranes.
B. Left, DAmFRET plot of $ASC^{PYD}$ expressed alone. Right, DAmFRET plot of $ASC^{PYD}$ co-expressed with FL NLRP3 showing persistence of the supersaturated bottom population indicating that FL NLRP3 oligomers are not active (in the absence of stimulation).

Figure S5. **Characterization of engineered THP-1 cell lines and apoptosome assembly, related to Figures 3 and 4**

A. DAmFRET plots of $APAF1^{CARD}$ and $CASP9^{CARD}$ measured in the presence of the indicated “seeds” expressed in trans. Both proteins fail to populate a high-AmFRET state.
B. Western blot verifying the knock-out status of ASC and/or FADD in the respective engineered stable THP-1 cell lines. Actin is the loading control.
C. Cartoon depicting the doxycycline-inducible ASC-mScarlet that replaced endogenous ASC in THP-1 *PYCARD-KO* cells.
D. Representative capillary Western blots comparing expression levels of the dox-inducible ASC-mScarlet construct alongside endogenous ASC. Actin is the loading control.
E. Quantification of the data showing significantly lower-than endogenous levels of ASC in the engineered construct at even the highest level of induction by Doxycycline. For each condition, 1 million cells were sorted and lysed.

Figure S6. **Generation and validation of the DFD nucleating interactome, related to Figure 5**

A. Illustration of how the library of all pairs of DFDs was created. An arrayed sublibrary of yeast transformed with 105 DFD-mEos3 fusions was mated to a separate arrayed

sublibrary of yeast strains expressing 107 chromosomally integrated DFD-μNS-mCardinal fusions, to create a library of 12,660 diploid strains representing all pairwise combinations.

B. Left, DAmFRET was run on all pairwise combinations. Only high quality datasets -- having a total cell count greater or equal to 2500 and a mean acceptor intensity greater or equal to 3.5 p.d.u. -- were used in the analysis. Right, DAmFRET plots of $FADD^{FL}$ either null-seeded (lacking a DFD) or self-seeded. Nucleating interactions (as shown by the self-seeded example) are indicated by a reduced EC50 and increased percentage of cells with self-assemblies (those above the gate delimiting low FRET, shown in orange).

C. Hits are determined by a multiparameter combination of the degree of EC50 outlier and the degree of fraction assembled outlier as defined by how many interquartile ranges (IQR) a plot is below or above the median, respectively. Points on the graph are shaded by this parameter. The leftmost set of boxplots show the distribution of standardized log10 EC50 and fraction assembled for all seeds for a representative protein, $FADD^{FL}$. The middle boxplot shows the average outlier degree value of these two parameters. This value is referred to as “seedability” throughout the text and is used in determining hits. The cutoff value for hit determination was set to be 3 standard deviations above the mean of all seedability values across the screen. The scatter plot on the right shows the standardized log10 EC50 and fraction assembled values, depicting the contribution of both to the scoring value and positive nucleating interactions within the green box.

D. Top, scatter plot of seedability values from the two replicate experiments containing 3478 DFD + seed combinations. Points are colored according to agreement between the two experiments. Gray rectangles indicate seedability values of negative interactions, with the dark gray square containing the interaction found to be negative for both instances. Bottom, the replicates after the removal of instances found to be negative in both experiments to reduce random and outlier effects. The line of best fit is shown in red. Pearson correlation R between the two experiments = 0.91 ($p < 0.0001$). In order to reduce the effects of random variations of the negatives as well as outlier effects, we omitted double negative instances. In this case, the Pearson correlation R = 0.90 ($p < 0.0001$).

E. 17 DFD + seed combinations that had inconsistent hit-calling out of the 3478 combinations reassessed. From this we determine that our assay had a consistency of 99.51% with a 95% confidence interval of 99.28 - 99.74%.

F. Bar plots showing the number of hits per experiment, as well as total number of hits, determined for each replicated DFD. Blue and yellow indicate separate hit counts for each experiment. Gray are the number of unique hits found across both experiments. What percentage of seeds are consistently called hits are shown for each DFD. The left bar plot shows the overall summary of all DFDs included in both sets.

**Figure S7. Bar plot of the Spearman R correlation between cell type transcript abundance and EC50 values of DFDs, related for Figure 6**

Transcript levels for each cell type were obtained from the single cell RNA dataset of the Human Protein Atlas.

# Supplementary Tables

Table S1. **Metadata, construct specifics, and data for the human DFDs analyzed in this study, related to Figures 1 and 2.**

ND (not determined). NA (not applicable/available). FL (full-length). [a]rhx1052 was found to be discontinuous in 1 of 4 independent experiments. [b]rhx1053 was found to be discontinuous in 1 of 3 independent experiments. [c]Our results suggest that this domain of DR6 be re-annotated as DED.

Table S2. **Metadata, construct specifics, and data for additional proteins analyzed in this study, related to Figure 2.**

FL (full-length). [a]Mutations were made to inactivate enzymatic activity for cell death effectors.

Table S3. **Specifics of lentivirus vectors used in this study, related to Figures 4 and 5.**

Table S4. **Nucleating interactome of DFDs, related to Figure 5.** Note that plasmids rhx2938, rhx1071, rhx2934, rhx1113, rhx1064, rhx2933, and rhx1368; and seeds from rhx2938, rhx2933 and rhx2934; did not pass quality control as outlined in methods and were therefore omitted from the analysis.

# Acknowledgements

We thank Mark Miller for assistance with illustrations. This work was performed to fulfill, in part, requirements for ARG's thesis research in the Graduate School of the Stowers Institute for Medical Research. This work was supported by the National Institute of General Medical Sciences (Award Number R01GM130927, to RH) and the National Institute on Aging (Award Number F99AG068511, to ARG) of the National Institutes of Health, the American Cancer Society (RSG-19-217-01-CCG to RH), and the Stowers Institute for Medical Research. The funders had no role in study design, data collection and analysis, or manuscript preparation. The content is solely the responsibility of the authors and does not necessarily represent the official views of the funders.

# Author Contributions

Conceptualization, A.R.G., S.V., and R.H.; Methodology, A.R.G., T.M., S.V., J.J.L., J.R.U. and R.H.; Formal Analysis, A.R.G., T.M., J.J.L. and J.R.U.; Investigation, A.R.G., T.M., S.V., J.J.L., J.W., X.S., and D.B.; Writing – Original Draft, A.R.G. and R.H.; Writing – Review & Editing, A.R.G., S.V., T.M. and R.H.; Funding Acquisition, A.R.G. and R.H.; Supervision, R.H.

# Declaration of Interests

The authors declare no competing interests.

# Data availability

Original data underlying this manuscript can be accessed from the Stowers Original Data Repository at http://www.stowers.org/research/publications/libpb-2387

Bibliography


1. Matyszewski, M., Morrone, S.R., and Sohn, J. (2018). Digital signaling network drives the assembly of the AIM2-ASC inflammasome. Proc Natl Acad Sci USA *115*, E1963–E1972. 10.1073/pnas.1712860115.
2. Sharma, M., and de Alba, E. (2022). Assembly mechanism of the AIM2 inflammasome sensor revealed by single-molecule analysis. BioRxiv. 10.1101/2022.09.21.508942.
3. Morrone, S.R., Matyszewski, M., Yu, X., Delannoy, M., Egelman, E.H., and Sohn, J. (2015). Assembly-driven activation of the AIM2 foreign-dsDNA sensor provides a polymerization template for downstream ASC. Nat. Commun. *6*, 7827. 10.1038/ncomms8827.
4. Stratmann, S.A., Morrone, S.R., van Oijen, A.M., and Sohn, J. (2015). The innate immune sensor IFI16 recognizes foreign DNA in the nucleus by scanning along the duplex. eLife *4*, e11721. 10.7554/eLife.11721.
5. Cadena, C., and Hur, S. (2019). Filament-like Assemblies of Intracellular Nucleic Acid Sensors: Commonalities and Differences. Mol. Cell *76*, 243–254. 10.1016/j.molcel.2019.09.023.
6. Jiang, Q.-X. (2019). Structural Variability in the RLR-MAVS Pathway and Sensitive Detection of Viral RNAs. Med. Chem. *15*, 443–458. 10.2174/1573406415666181219101613.
7. Latty, S.L., Sakai, J., Hopkins, L., Verstak, B., Paramo, T., Berglund, N.A., Cammarota, E., Cicuta, P., Gay, N.J., Bond, P.J., et al. (2018). Activation of Toll-like receptors nucleates assembly of the MyDDosome signaling hub. eLife *7*. 10.7554/eLife.31377.
8. Kaur, G., Iyer, L.M., Burroughs, A.M., and Aravind, L. (2021). Bacterial death and TRADD-N domains help define novel apoptosis and immunity mechanisms shared by prokaryotes and metazoans. eLife *10*. 10.7554/eLife.70394.
9. Dyrka, W., Coustou, V., Daskalov, A., Lends, A., Bardin, T., Berbon, M., Kauffmann, B.,

Blancard, C., Salin, B., Loquet, A., et al. (2020). Identification of NLR-associated Amyloid Signaling Motifs in Bacterial Genomes. J. Mol. Biol. *432*, 6005–6027. 10.1016/j.jmb.2020.10.004.

10. Kibby, E.M., Conte, A.N., Burroughs, A.M., Nagy, T.A., Vargas, J.A., Whalen, L.A., Aravind, L., and Whiteley, A.T. (2023). Bacterial NLR-related proteins protect against phage. Cell *186*, 2410-2424.e18. 10.1016/j.cell.2023.04.015.

11. Wein, T., Johnson, A.G., Millman, A., Lange, K., Yirmiya, E., Hadary, R., Garb, J., Steinruecke, F., Hill, A.B., Kranzusch, P.J., et al. (2023). CARD-like domains mediate anti-phage defense in bacterial gasdermin systems. BioRxiv. 10.1101/2023.05.28.542683.

12. Mehta, P., Lang, A.H., and Schwab, D.J. (2016). Landauer in the age of synthetic biology: energy consumption and information processing in biochemical networks. J. Stat. Phys. *162*, 1153–1166. 10.1007/s10955-015-1431-6.

13. Bérut, A., Arakelyan, A., Petrosyan, A., Ciliberto, S., Dillenschneider, R., and Lutz, E. (2012). Experimental verification of Landauer's principle linking information and thermodynamics. Nature *483*, 187–189. 10.1038/nature10872.

14. Goldbeter, A., and Koshland, D.E. (1981). An amplified sensitivity arising from covalent modification in biological systems. Proc Natl Acad Sci USA *78*, 6840–6844. 10.1073/pnas.78.11.6840.

15. Franklin, B.S., Bossaller, L., De Nardo, D., Ratter, J.M., Stutz, A., Engels, G., Brenker, C., Nordhoff, M., Mirandola, S.R., Al-Amoudi, A., et al. (2014). The adaptor ASC has extracellular and "prionoid" activities that propagate inflammation. Nat. Immunol. *15*, 727–737. 10.1038/ni.2913.

16. Cai, X., Chen, J., Xu, H., Liu, S., Jiang, Q.-X., Halfmann, R., and Chen, Z.J. (2014). Prion-like polymerization underlies signal transduction in antiviral immune defense and inflammasome activation. Cell *156*, 1207–1222. 10.1016/j.cell.2014.01.063.

17. Hou, F., Sun, L., Zheng, H., Skaug, B., Jiang, Q.-X., and Chen, Z.J. (2011). MAVS forms functional prion-like aggregates to activate and propagate antiviral innate immune response. Cell *146*, 448–461. 10.1016/j.cell.2011.06.041.

18. Lu, A., Magupalli, V.G., Ruan, J., Yin, Q., Atianand, M.K., Vos, M.R., Schröder, G.F., Fitzgerald, K.A., Wu, H., and Egelman, E.H. (2014). Unified polymerization mechanism for the assembly of ASC-dependent inflammasomes. Cell *156*, 1193–1206. 10.1016/j.cell.2014.02.008.

19. Holliday, M.J., Witt, A., Rodríguez Gama, A., Walters, B.T., Arthur, C.P., Halfmann, R., Rohou, A., Dueber, E.C., and Fairbrother, W.J. (2019). Structures of autoinhibited and polymerized forms of CARD9 reveal mechanisms of CARD9 and CARD11 activation. Nat. Commun. *10*, 3070. 10.1038/s41467-019-10953-z.

20. Qiao, Q., Yang, C., Zheng, C., Fontán, L., David, L., Yu, X., Bracken, C., Rosen, M., Melnick, A., Egelman, E.H., et al. (2013). Structural architecture of the CARMA1/Bcl10/MALT1 signalosome: nucleation-induced filamentous assembly. Mol. Cell *51*, 766–779. 10.1016/j.molcel.2013.08.032.

21. Wu, H. (2013). Higher-order assemblies in a new paradigm of signal transduction. Cell *153*, 287–292. 10.1016/j.cell.2013.03.013.

22. O'Carroll, A., Coyle, J., and Gambin, Y. (2020). Prions and Prion-like assemblies in neurodegeneration and immunity: The emergence of universal mechanisms across health and disease. Semin. Cell Dev. Biol. *99*, 115–130. 10.1016/j.semcdb.2019.11.012.

23. Nanson, J.D., Kobe, B., and Ve, T. (2019). Death, TIR, and RHIM: Self-assembling domains involved in innate immunity and cell-death signaling. J. Leukoc. Biol. *105*, 363–375. 10.1002/JLB.MR0318-123R.

24. Kagan, J.C., Magupalli, V.G., and Wu, H. (2014). SMOCs: supramolecular organizing centres that control innate immunity. Nat. Rev. Immunol. *14*, 821–826. 10.1038/nri3757.

25. Dick, M.S., Sborgi, L., Rühl, S., Hiller, S., and Broz, P. (2016). ASC filament formation serves as a signal amplification mechanism for inflammasomes. Nat. Commun. *7*, 11929. 10.1038/ncomms11929.

26. Shkarina, K., Hasel de Carvalho, E., Santos, J.C., Ramos, S., Leptin, M., and Broz, P. (2022). Optogenetic activators of apoptosis, necroptosis, and pyroptosis. J. Cell Biol. *221*. 10.1083/jcb.202109038.

27. Rodríguez Gama, A., Miller, T., and Halfmann, R. (2021). Mechanics of a molecular mousetrap-nucleation-limited innate immune signaling. Biophys. J. *120*, 1150–1160. 10.1016/j.bpj.2021.01.007.

28. David, L., Li, Y., Ma, J., Garner, E., Zhang, X., and Wu, H. (2018). Assembly mechanism of the CARMA1-BCL10-MALT1-TRAF6 signalosome. Proc Natl Acad Sci USA *115*, 1499–1504. 10.1073/pnas.1721967115.

29. Su, T.-W., Yang, C.-Y., Kao, W.-P., Kuo, B.-J., Lin, S.-M., Lin, J.-Y., Lo, Y.-C., and Lin, S.-C. (2017). Structural Insights into DD-Fold Assembly and Caspase-9 Activation by the Apaf-1 Apoptosome. Structure *25*, 407–420. 10.1016/j.str.2016.12.019.

30. Devi, S., Stehlik, C., and Dorfleutner, A. (2020). An update on CARD only proteins (cops) and PYD only proteins (pops) as inflammasome regulators. Int. J. Mol. Sci. *21*. 10.3390/ijms21186901.

31. Ohto, U., Kamitsukasa, Y., Ishida, H., Zhang, Z., Murakami, K., Hirama, C., Maekawa, S., and Shimizu, T. (2022). Structural basis for the oligomerization-mediated regulation of NLRP3 inflammasome activation. Proc Natl Acad Sci USA *119*, e2121353119. 10.1073/pnas.2121353119.

32. Hochheiser, I.V., Pilsl, M., Hagelueken, G., Moecking, J., Marleaux, M., Brinkschulte, R., Latz, E., Engel, C., and Geyer, M. (2022). Structure of the NLRP3 decamer bound to the cytokine release inhibitor CRID3. Nature *604*, 184–189. 10.1038/s41586-022-04467-w.

33. Sommer, K., Guo, B., Pomerantz, J.L., Bandaranayake, A.D., Moreno-García, M.E., Ovechkina, Y.L., and Rawlings, D.J. (2005). Phosphorylation of the CARMA1 linker controls NF-kappaB activation. Immunity *23*, 561–574. 10.1016/j.immuni.2005.09.014.

34. Andreeva, L., David, L., Rawson, S., Shen, C., Pasricha, T., Pelegrin, P., and Wu, H.

(2021). NLRP3 cages revealed by full-length mouse NLRP3 structure control pathway activation. Cell *184*, 6299-6312.e22. 10.1016/j.cell.2021.11.011.

35. Chuenchor, W., Jin, T., Ravilious, G., and Xiao, T.S. (2014). Structures of pattern recognition receptors reveal molecular mechanisms of autoinhibition, ligand recognition and oligomerization. Curr. Opin. Immunol. *26*, 14–20. 10.1016/j.coi.2013.10.009.

36. Huoh, Y.-S., and Hur, S. (2022). Death domain fold proteins in immune signaling and transcriptional regulation. FEBS J. *289*, 4082–4097. 10.1111/febs.15901.

37. Anfinsen, C.B. (1973). Principles that govern the folding of protein chains. Science *181*, 223–230. 10.1126/science.181.4096.223.

38. Frauenfelder, H., Sligar, S.G., and Wolynes, P.G. (1991). The energy landscapes and motions of proteins. Science *254*, 1598–1603. 10.1126/science.1749933.

39. Lee, C., Park, S.H., Lee, M.Y., and Yu, M.H. (2000). Regulation of protein function by native metastability. Proc Natl Acad Sci USA *97*, 7727–7731. 10.1073/pnas.97.14.7727.

40. Carr, C.M., and Kim, P.S. (1993). A spring-loaded mechanism for the conformational change of influenza hemagglutinin. Cell *73*, 823–832. 10.1016/0092-8674(93)90260-w.

41. Vekilov, P.G. (2012). Phase diagrams and kinetics of phase transitions in protein solutions. J. Phys. Condens. Matter *24*, 193101. 10.1088/0953-8984/24/19/193101.

42. Buell, A.K. (2017). The Nucleation of Protein Aggregates - From Crystals to Amyloid Fibrils. Int. Rev. Cell Mol. Biol. *329*, 187–226. 10.1016/bs.ircmb.2016.08.014.

43. Khan, T., Kandola, T.S., Wu, J., Venkatesan, S., Ketter, E., Lange, J.J., Rodríguez Gama, A., Box, A., Unruh, J.R., Cook, M., et al. (2018). Quantifying nucleation in vivo reveals the physical basis of prion-like phase behavior. Mol. Cell *71*, 155-168.e7. 10.1016/j.molcel.2018.06.016.

44. Jarrett, J.T., and Lansbury, P.T. (1993). Seeding “one-dimensional crystallization” of amyloid: a pathogenic mechanism in Alzheimer’s disease and scrapie? Cell *73*, 1055–1058. 10.1016/0092-8674(93)90635-4.

45. Prusiner, S.B., McKinley, M.P., Bowman, K.A., Bolton, D.C., Bendheim, P.E., Groth, D.F., and Glenner, G.G. (1983). Scrapie prions aggregate to form amyloid-like birefringent rods. Cell *35*, 349–358. 10.1016/0092-8674(83)90168-x.

46. Rodriguez Gama, A., Miller, T., Lange, J.J., Unruh, J.R., and Halfmann, R. (2022). A nucleation barrier spring-loads the CBM signalosome for binary activation. eLife *11*. 10.7554/eLife.79826.

47. Capra, E.J., Perchuk, B.S., Skerker, J.M., and Laub, M.T. (2012). Adaptive mutations that prevent crosstalk enable the expansion of paralogous signaling protein families. Cell *150*, 222–232. 10.1016/j.cell.2012.05.033.

48. Zarrinpar, A., Park, S.-H., and Lim, W.A. (2003). Optimization of specificity in a cellular protein interaction network by negative selection. Nature *426*, 676–680. 10.1038/nature02178.

49. Lizana, J., Sanchez-Jimenez, P.E., Chacartegui, R., Becerra, J.A., and Perez-Maqueda,

L.A. (2022). Supercooled sodium acetate aqueous solution for long-term heat storage to support heating decarbonisation. Journal of Energy Storage *55*, 105584. 10.1016/j.est.2022.105584.

50. Sharma, A., Tyagi, V.V., Chen, C.R., and Buddhi, D. (2009). Review on thermal energy storage with phase change materials and applications. Renew. Sustain. Energy Rev *13*, 318–345. 10.1016/j.rser.2007.10.005.

51. Varadi, M., Anyango, S., Deshpande, M., Nair, S., Natassia, C., Yordanova, G., Yuan, D., Stroe, O., Wood, G., Laydon, A., et al. (2022). AlphaFold Protein Structure Database: massively expanding the structural coverage of protein-sequence space with high-accuracy models. Nucleic Acids Res. *50*, D439–D444. 10.1093/nar/gkab1061.

52. Zhang, M., Chang, H., Zhang, Y., Yu, J., Wu, L., Ji, W., Chen, J., Liu, B., Lu, J., Liu, Y., et al. (2012). Rational design of true monomeric and bright photoactivatable fluorescent proteins. Nat. Methods *9*, 727–729. 10.1038/nmeth.2021.

53. Kandola, T., Venkatesan, S., Zhang, J., Lerbakken, B.T., Von Schulze, A., Blanck, J.F., Wu, J., Unruh, J.R., Berry, P., Lange, J.J., et al. (2023). Pathologic polyglutamine aggregation begins with a self-poisoning polymer crystal. eLife *12*. 10.7554/eLife.86939.

54. Posey, A.E., Ruff, K.M., Lalmansingh, J.M., Kandola, T.S., Lange, J.J., Halfmann, R., and Pappu, R.V. (2021). Mechanistic inferences from analysis of measurements of protein phase transitions in live cells. J. Mol. Biol. *433*, 166848. 10.1016/j.jmb.2021.166848.

55. Shearwin-Whyatt, L.M., Harvey, N.L., and Kumar, S. (2000). Subcellular localization and CARD-dependent oligomerization of the death adaptor RAIDD. Cell Death Differ. *7*, 155–165. 10.1038/sj.cdd.4400632.

56. Schmitz, A.M., Morrison, M.F., Agunwamba, A.O., Nibert, M.L., and Lesser, C.F. (2009). Protein interaction platforms: visualization of interacting proteins in yeast. Nat. Methods *6*, 500–502. 10.1038/nmeth.1337.

57. Miller, T., Wu, J., Venkatesan, S., Gama, A.R., and Halfmann, R. (2023). DAmFRET measures saturating concentrations and toxicities of protein phase transitions in vivo. Mol. Biol. Cell, mbcE22110503. 10.1091/mbc.E22-11-0503.

58. Halfmann, R., and Lindquist, S. (2008). Screening for amyloid aggregation by Semi-Denaturing Detergent-Agarose Gel Electrophoresis. J. Vis. Exp. *17*, e838. 10.3791/838.

59. Kar, M., Dar, F., Welsh, T.J., Vogel, L.T., Kühnemuth, R., Majumdar, A., Krainer, G., Franzmann, T.M., Alberti, S., Seidel, C.A.M., et al. (2022). Phase-separating RNA-binding proteins form heterogeneous distributions of clusters in subsaturated solutions. Proc Natl Acad Sci USA *119*, e2202222119. 10.1073/pnas.2202222119.

60. Vecchi, G., Sormanni, P., Mannini, B., Vandelli, A., Tartaglia, G.G., Dobson, C.M., Hartl, F.U., and Vendruscolo, M. (2020). Proteome-wide observation of the phenomenon of life on the edge of solubility. Proc Natl Acad Sci USA *117*, 1015–1020. 10.1073/pnas.1910444117.

61. Wang, M., Herrmann, C.J., Simonovic, M., Szklarczyk, D., and von Mering, C. (2015). Version 4.0 of PaxDb: Protein abundance data, integrated across model organisms,

tissues, and cell-lines. Proteomics *15*, 3163–3168. 10.1002/pmic.201400441.

62. Karlsson, M., Zhang, C., Méar, L., Zhong, W., Digre, A., Katona, B., Sjöstedt, E., Butler, L., Odeberg, J., Dusart, P., et al. (2021). A single-cell type transcriptomics map of human tissues. Sci. Adv. *7*. 10.1126/sciadv.abh2169.

63. Uhlen, M., Karlsson, M.J., Zhong, W., Tebani, A., Pou, C., Mikes, J., Lakshmikanth, T., Forsström, B., Edfors, F., Odeberg, J., et al. (2019). A genome-wide transcriptomic analysis of protein-coding genes in human blood cells. Science *366*. 10.1126/science.aax9198.

64. Jeong, H., Mason, S.P., Barabási, A.L., and Oltvai, Z.N. (2001). Lethality and centrality in protein networks. Nature *411*, 41–42. 10.1038/35075138.

65. Nithya, C., Kiran, M., and Nagarajaram, H.A. (2022). Dissection of hubs and bottlenecks in a Protein-protein Interaction Network. Comput. Biol. Chem., 107802. 10.1016/j.compbiolchem.2022.107802.

66. Pang, E., Hao, Y., Sun, Y., and Lin, K. (2016). Differential variation patterns between hubs and bottlenecks in human protein-protein interaction networks. BMC Evol. Biol. *16*, 260. 10.1186/s12862-016-0840-8.

67. Schleker, S., and Trilling, M. (2013). Data-warehousing of protein-protein interactions indicates that pathogens preferentially target hub and bottleneck proteins. Front. Microbiol. *4*, 51. 10.3389/fmicb.2013.00051.

68. Szklarczyk, D., Kirsch, R., Koutrouli, M., Nastou, K., Mehryary, F., Hachilif, R., Gable, A.L., Fang, T., Doncheva, N.T., Pyysalo, S., et al. (2023). The STRING database in 2023: protein-protein association networks and functional enrichment analyses for any sequenced genome of interest. Nucleic Acids Res. *51*, D638–D646. 10.1093/nar/gkac1000.

69. Gong, Y.-N., Crawford, J.C., Heckmann, B.L., and Green, D.R. (2019). To the edge of cell death and back. FEBS J. *286*, 430–440. 10.1111/febs.14714.

70. Nano, M., Mondo, J.A., Harwood, J., Balasanyan, V., and Montell, D.J. (2023). Cell survival following direct executioner-caspase activation. Proc Natl Acad Sci USA *120*, e2216531120. 10.1073/pnas.2216531120.

71. Häcker, G., and Haimovici, A. (2023). Sub-lethal signals in the mitochondrial apoptosis apparatus: pernicious by-product or physiological event? Cell Death Differ. *30*, 250–257. 10.1038/s41418-022-01058-0.

72. Park, H., Kim, N.Y., Lee, S., Kim, N., Kim, J., and Heo, W.D. (2017). Optogenetic protein clustering through fluorescent protein tagging and extension of CRY2. Nat. Commun. *8*, 30. 10.1038/s41467-017-00060-2.

73. Kennedy, M.J., Hughes, R.M., Peteya, L.A., Schwartz, J.W., Ehlers, M.D., and Tucker, C.L. (2010). Rapid blue-light-mediated induction of protein interactions in living cells. Nat. Methods *7*, 973–975. 10.1038/nmeth.1524.

74. Sagulenko, V., Thygesen, S.J., Sester, D.P., Idris, A., Cridland, J.A., Vajjhala, P.R.,

Roberts, T.L., Schroder, K., Vince, J.E., Hill, J.M., et al. (2013). AIM2 and NLRP3 inflammasomes activate both apoptotic and pyroptotic death pathways via ASC. Cell Death Differ. *20*, 1149–1160. 10.1038/cdd.2013.37.

75. Fritsch, M., Günther, S.D., Schwarzer, R., Albert, M.-C., Schorn, F., Werthenbach, J.P., Schiffmann, L.M., Stair, N., Stocks, H., Seeger, J.M., et al. (2019). Caspase-8 is the molecular switch for apoptosis, necroptosis and pyroptosis. Nature *575*, 683–687. 10.1038/s41586-019-1770-6.

76. Bedoui, S., Herold, M.J., and Strasser, A. (2020). Emerging connectivity of programmed cell death pathways and its physiological implications. Nat. Rev. Mol. Cell Biol. *21*, 678–695. 10.1038/s41580-020-0270-8.

77. Snyder, A.G., and Oberst, A. (2021). The antisocial network: cross talk between cell death programs in host defense. Annu. Rev. Immunol. *39*, 77–101. 10.1146/annurev-immunol-112019-072301.

78. Gullett, J.M., Tweedell, R.E., and Kanneganti, T.-D. (2022). It's All in the PAN: Crosstalk, Plasticity, Redundancies, Switches, and Interconnectedness Encompassed by PANoptosis Underlying the Totality of Cell Death-Associated Biological Effects. Cells *11*. 10.3390/cells11091495.

79. Christgen, S., Zheng, M., Kesavardhana, S., Karki, R., Malireddi, R.K.S., Banoth, B., Place, D.E., Briard, B., Sharma, B.R., Tuladhar, S., et al. (2020). Identification of the panoptosome: A molecular platform triggering pyroptosis, apoptosis, and necroptosis (panoptosis). Front. Cell. Infect. Microbiol. *10*, 237. 10.3389/fcimb.2020.00237.

80. Maelfait, J., Liverpool, L., and Rehwinkel, J. (2020). Nucleic acid sensors and programmed cell death. J. Mol. Biol. *432*, 552–568. 10.1016/j.jmb.2019.11.016.

81. Place, D.E., Christgen, S., Tuladhar, S., Vogel, P., Malireddi, R.K.S., and Kanneganti, T.-D. (2021). Hierarchical Cell Death Program Disrupts the Intracellular Niche Required for Burkholderia thailandensis Pathogenesis. MBio *12*, e0105921. 10.1128/mBio.01059-21.

82. Roncaioli, J.L., Babirye, J.P., Chavez, R.A., Liu, F.L., Turcotte, E.A., Lee, A.Y., Lesser, C.F., and Vance, R.E. (2023). A hierarchy of cell death pathways confers layered resistance to shigellosis in mice. eLife *12*. 10.7554/eLife.83639.

83. Tummers, B., Mari, L., Guy, C.S., Heckmann, B.L., Rodriguez, D.A., Rühl, S., Moretti, J., Crawford, J.C., Fitzgerald, P., Kanneganti, T.-D., et al. (2020). Caspase-8-Dependent Inflammatory Responses Are Controlled by Its Adaptor, FADD, and Necroptosis. Immunity *52*, 994-1006.e8. 10.1016/j.immuni.2020.04.010.

84. Bindels, D.S., Haarbosch, L., van Weeren, L., Postma, M., Wiese, K.E., Mastop, M., Aumonier, S., Gotthard, G., Royant, A., Hink, M.A., et al. (2017). mScarlet: a bright monomeric red fluorescent protein for cellular imaging. Nat. Methods *14*, 53–56. 10.1038/nmeth.4074.

85. Chertkova, A.O., Mastop, M., Postma, M., van Bommel, N., van der Niet, S., Batenburg, K.L., Joosen, L., Gadella, T.W.J., Okada, Y., and Goedhart, J. (2017). Robust and bright genetically encoded fluorescent markers for highlighting structures and compartments in

mammalian cells. BioRxiv. 10.1101/160374.

86. He, W., Wan, H., Hu, L., Chen, P., Wang, X., Huang, Z., Yang, Z.-H., Zhong, C.-Q., and Han, J. (2015). Gasdermin D is an executor of pyroptosis and required for interleukin-1β secretion. Cell Res. *25*, 1285–1298. 10.1038/cr.2015.139.

87. Boucher, D., Monteleone, M., Coll, R.C., Chen, K.W., Ross, C.M., Teo, J.L., Gomez, G.A., Holley, C.L., Bierschenk, D., Stacey, K.J., et al. (2018). Caspase-1 self-cleavage is an intrinsic mechanism to terminate inflammasome activity. J. Exp. Med. *215*, 827–840. 10.1084/jem.20172222.

88. Gambin, Y., Giles, N., O'Carroll, A., Polinkovsky, M., Hunter, D., and Sierecki, E. (2018). Single-Molecule Fluorescence Reveals the Oligomerization and Folding Steps Driving the Prion-like Behavior of ASC. J. Mol. Biol. *430*, 491–508. 10.1016/j.jmb.2017.12.013.

89. Park, H.H., Lo, Y.-C., Lin, S.-C., Wang, L., Yang, J.K., and Wu, H. (2007). The death domain superfamily in intracellular signaling of apoptosis and inflammation. Annu. Rev. Immunol. *25*, 561–586. 10.1146/annurev.immunol.25.022106.141656.

90. Qi, N., Shi, Y., Zhang, R., Zhu, W., Yuan, B., Li, X., Wang, C., Zhang, X., and Hou, F. (2017). Multiple truncated isoforms of MAVS prevent its spontaneous aggregation in antiviral innate immune signalling. Nat. Commun. *8*, 15676. 10.1038/ncomms15676.

91. Lin, S.-C., Lo, Y.-C., and Wu, H. (2010). Helical assembly in the MyD88-IRAK4-IRAK2 complex in TLR/IL-1R signalling. Nature *465*, 885–890. 10.1038/nature09121.

92. Moncrieffe, M.C., Bollschweiler, D., Li, B., Penczek, P.A., Hopkins, L., Bryant, C.E., Klenerman, D., and Gay, N.J. (2020). MyD88 Death-Domain Oligomerization Determines Myddosome Architecture: Implications for Toll-like Receptor Signaling. Structure *28*, 281-289.e3. 10.1016/j.str.2020.01.003.

93. Clabbers, M.T.B., Holmes, S., Muusse, T.W., Vajjhala, P.R., Thygesen, S.J., Malde, A.K., Hunter, D.J.B., Croll, T.I., Flueckiger, L., Nanson, J.D., et al. (2021). MyD88 TIR domain higher-order assembly interactions revealed by microcrystal electron diffraction and serial femtosecond crystallography. Nat. Commun. *12*, 2578. 10.1038/s41467-021-22590-6.

94. Rajpoot, S., Wary, K.K., Ibbott, R., Liu, D., Saqib, U., Thurston, T.L.M., and Baig, M.S. (2021). TIRAP in the mechanism of inflammation. Front. Immunol. *12*, 697588. 10.3389/fimmu.2021.697588.

95. Horng, T., Barton, G.M., Flavell, R.A., and Medzhitov, R. (2002). The adaptor molecule TIRAP provides signalling specificity for Toll-like receptors. Nature *420*, 329–333. 10.1038/nature01180.

96. Lannoy, V., Côté-Biron, A., Asselin, C., and Rivard, N. (2023). TIRAP, TRAM, and Toll-Like Receptors: The Untold Story. Mediators Inflamm. *2023*, 2899271. 10.1155/2023/2899271.

97. Bonham, K.S., Orzalli, M.H., Hayashi, K., Wolf, A.I., Glanemann, C., Weninger, W., Iwasaki, A., Knipe, D.M., and Kagan, J.C. (2014). A promiscuous lipid-binding protein diversifies the subcellular sites of toll-like receptor signal transduction. Cell *156*, 705–716. 10.1016/j.cell.2014.01.019.

98. Ve, T., Vajjhala, P.R., Hedger, A., Croll, T., DiMaio, F., Horsefield, S., Yu, X., Lavrencic, P., Hassan, Z., Morgan, G.P., et al. (2017). Structural basis of TIR-domain-assembly formation in MAL- and MyD88-dependent TLR4 signaling. Nat. Struct. Mol. Biol. *24*, 743–751. 10.1038/nsmb.3444.

99. Deliz-Aguirre, R., Cao, F., Gerpott, F.H.U., Auevechanichkul, N., Chupanova, M., Mun, Y., Ziska, E., and Taylor, M.J. (2021). MyD88 oligomer size functions as a physical threshold to trigger IL1R Myddosome signaling. J. Cell Biol. *220*. 10.1083/jcb.202012071.

100. Pustelny, K., Kuska, K., Gorecki, A., Musielak, B., Dobosz, E., Wladyka, B., Koziel, J., Czarna, A., Holak, T., and Dubin, G. (2022). Mechanism of MyD88S mediated signal termination. Cell Commun. Signal. *20*, 10. 10.1186/s12964-021-00811-1.

101. O'Carroll, A., Chauvin, B., Brown, J.W.P., Meagher, A., Coyle, J., Schill, J., Bhumkhar, A., Hunter, D.J.B., Ve, T., Kobe, B., et al. (2018). Pathological mutations differentially affect the self-assembly and polymerisation of the innate immune system signalling adaptor molecule MyD88. BMC Biol. *16*, 149. 10.1186/s12915-018-0611-7.

102. Weiler, E.S., Szabo, T.G., Garcia-Carpio, I., and Villunger, A. (2022). PIDD1 in cell cycle control, sterile inflammation and cell death. Biochem. Soc. Trans. *50*, 813–824. 10.1042/BST20211186.

103. Elmore, S. (2007). Apoptosis: a review of programmed cell death. Toxicol. Pathol. *35*, 495–516. 10.1080/01926230701320337.

104. Bienz, M. (2020). Head-to-tail polymerization in the assembly of biomolecular condensates. Cell *182*, 799–811. 10.1016/j.cell.2020.07.037.

105. Marks, F., Klingmüller, U., and Müller-Decker, K. (2017). Cellular signal processing: an introduction to the molecular mechanisms of signal transduction (Garland Science) 10.4324/9781315165479.

106. Pradel, B., Robert-Hebmann, V., and Espert, L. (2020). Regulation of innate immune responses by autophagy: A goldmine for viruses. Front. Immunol. *11*, 578038. 10.3389/fimmu.2020.578038.

107. Barton, J.P., and Sontag, E.D. (2013). The energy costs of insulators in biochemical networks. Biophys. J. *104*, 1380–1390. 10.1016/j.bpj.2013.01.056.

108. Dobson, C.M. (2003). Protein folding and misfolding. Nature *426*, 884–890. 10.1038/nature02261.

109. Garcia-Seisdedos, H., Empereur-Mot, C., Elad, N., and Levy, E.D. (2017). Proteins evolve on the edge of supramolecular self-assembly. Nature *548*, 244–247. 10.1038/nature23320.

110. De Greef, T.F.A., Smulders, M.M.J., Wolffs, M., Schenning, A.P.H.J., Sijbesma, R.P., and Meijer, E.W. (2009). Supramolecular polymerization. Chem. Rev. *109*, 5687–5754. 10.1021/cr900181u.

111. O'Flynn, B.G., and Mittag, T. (2021). The role of liquid-liquid phase separation in regulating enzyme activity. Curr. Opin. Cell Biol. *69*, 70–79. 10.1016/j.ceb.2020.12.012.

112. Shen, C., Li, R., Negro, R., Cheng, J., Vora, S.M., Fu, T.-M., Wang, A., He, K., Andreeva, L., Gao, P., et al. (2021). Phase separation drives RNA virus-induced activation of the NLRP6 inflammasome. Cell *184*, 5759-5774.e20. 10.1016/j.cell.2021.09.032.

113. Liu, D., Lum, K.K., Treen, N., Núñez, C.T., Yang, J., Howard, T.R., Levine, M., and Cristea, I.M. (2023). IFI16 phase separation via multi-phosphorylation drives innate immune signaling. Nucleic Acids Res. *51*, 6819–6840. 10.1093/nar/gkad449.

114. López-Otín, C., Blasco, M.A., Partridge, L., Serrano, M., and Kroemer, G. (2023). Hallmarks of aging: An expanding universe. Cell *186*, 243–278. 10.1016/j.cell.2022.11.001.

115. Sender, R., and Milo, R. (2021). The distribution of cellular turnover in the human body. Nat. Med. *27*, 45–48. 10.1038/s41591-020-01182-9.

116. Song, N., Liu, Z.-S., Xue, W., Bai, Z.-F., Wang, Q.-Y., Dai, J., Liu, X., Huang, Y.-J., Cai, H., Zhan, X.-Y., et al. (2017). NLRP3 phosphorylation is an essential priming event for inflammasome activation. Mol. Cell *68*, 185-197.e6. 10.1016/j.molcel.2017.08.017.

117. Gack, M.U., Shin, Y.C., Joo, C.-H., Urano, T., Liang, C., Sun, L., Takeuchi, O., Akira, S., Chen, Z., Inoue, S., et al. (2007). TRIM25 RING-finger E3 ubiquitin ligase is essential for RIG-I-mediated antiviral activity. Nature *446*, 916–920. 10.1038/nature05732.

118. Stringer, C., Wang, T., Michaelos, M., and Pachitariu, M. (2021). Cellpose: a generalist algorithm for cellular segmentation. Nat. Methods *18*, 100–106. 10.1038/s41592-020-01018-x.

Figure1

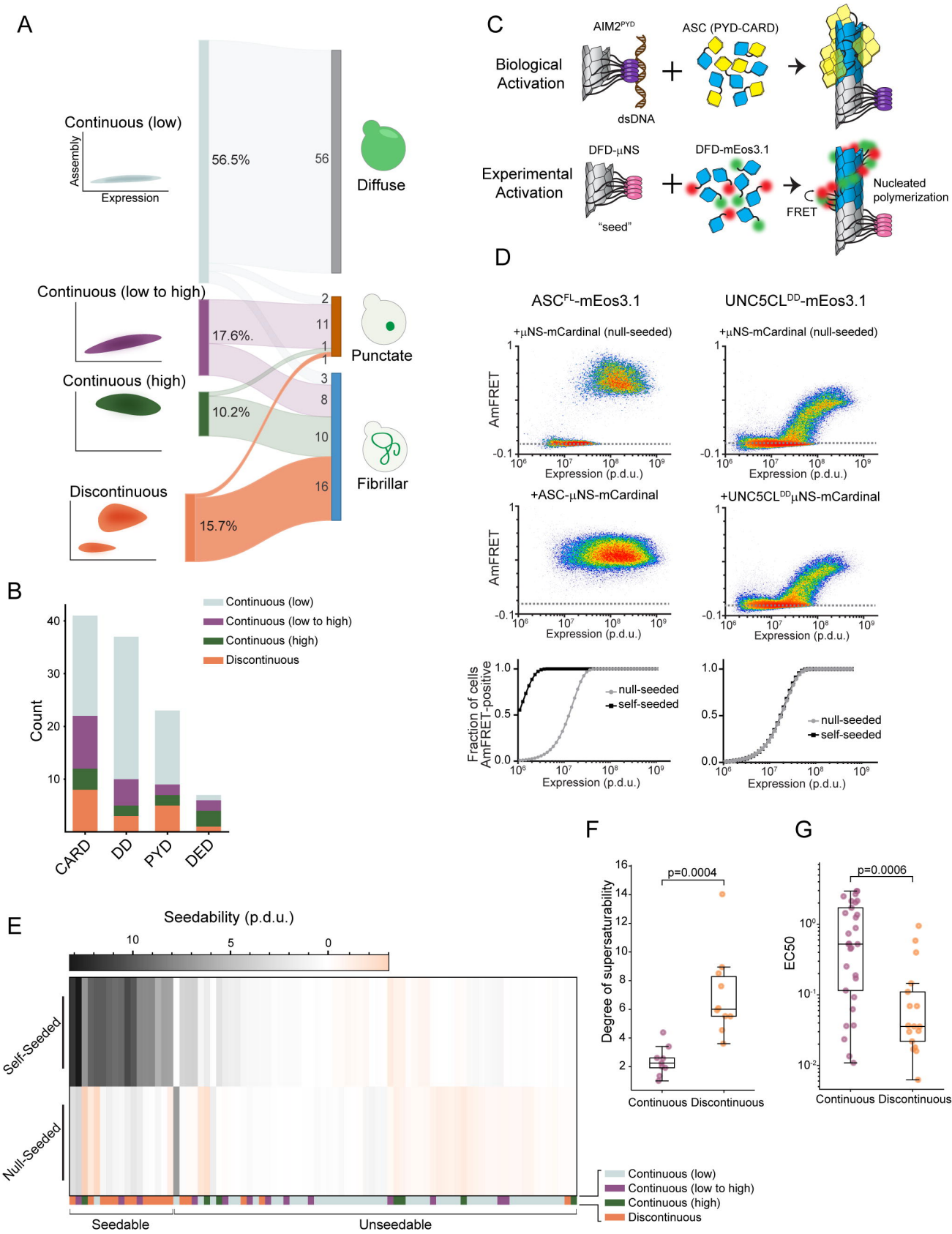
A
Continuous (low)
Assembly
Expression
56.5%
56
Diffuse
Continuous (low to high)
17.6%.
2
11
1
1
Punctate
Continuous (high)
10.2%
3
8
10
Fibrillar
Discontinuous
15.7%
16
B
Continuous (low)
Continuous (low to high)
Continuous (high)
Discontinuous
Count
CARD
DD
PYD
DED
C
Biological Activation
AIM2PYD
dsDNA
ASC (PYD-CARD)
Experimental Activation
DFD-μNS
"seed"
DFD-mEos3.1
FRET
Nucleated polymerization
D
ASCFL-mEos3.1
UNC5CLDD-mEos3.1
+μNS-mCardinal (null-seeded)
+ASC-μNS-mCardinal
+UNC5CLDDμNS-mCardinal
AmFRET
Expression (p.d.u.)
Fraction of cells AmFRET-positive
null-seeded
self-seeded
E
Seedability (p.d.u.)
Self-Seeded
Null-Seeded
Seedable
Unseedable
Continuous (low)
Continuous (low to high)
Continuous (high)
Discontinuous
F
p=0.0004
Degree of supersaturability
Continuous
Discontinuous
G
p=0.0006
EC50
Continuous
Discontinuous

Figure 2

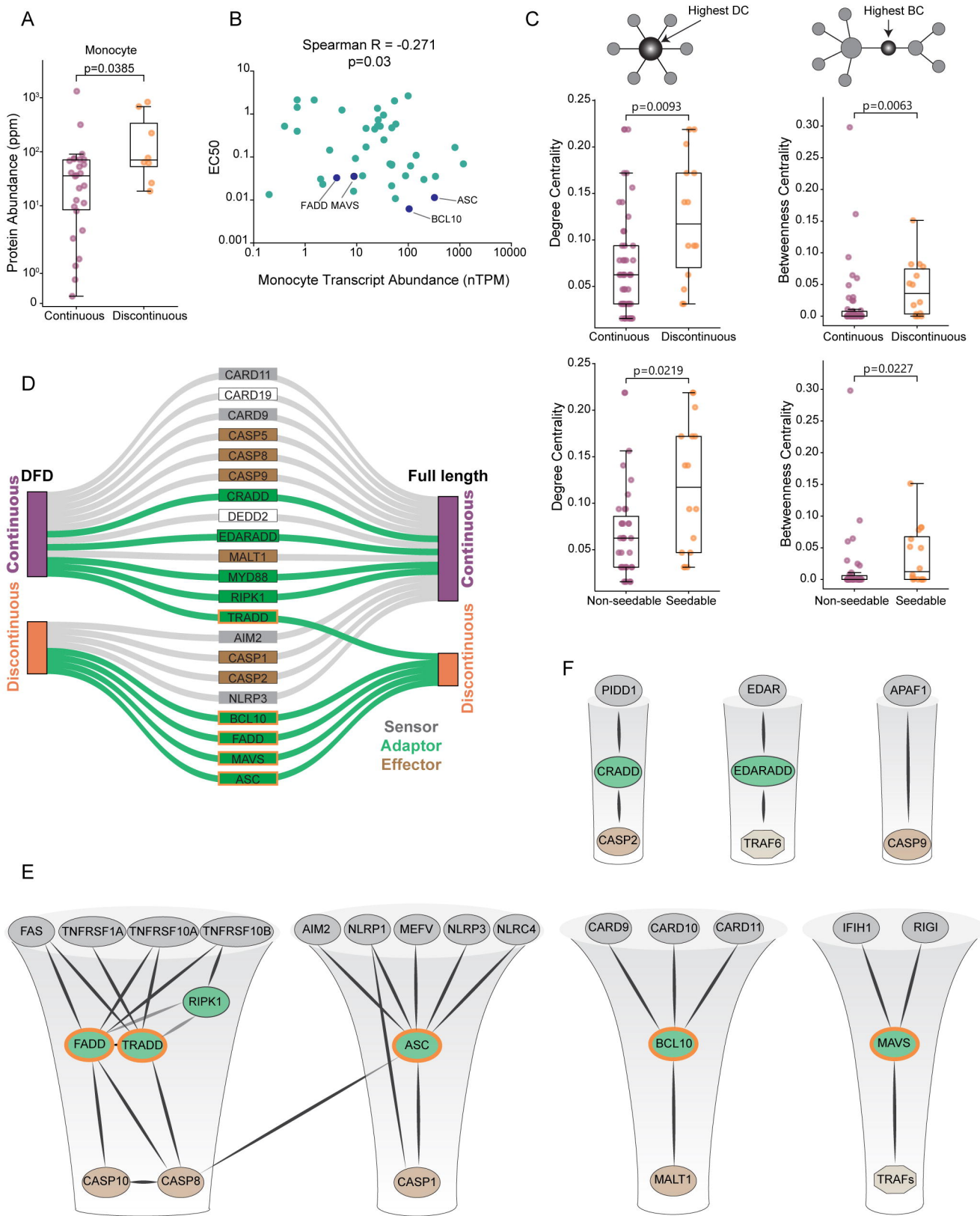
A
Monocyte
p=0.0385
Protein Abundance (ppm)
Continuous
Discontinuous
B
Spearman R = -0.271
p=0.03
EC50
FADD MAVS
ASC
BCL10
Monocyte Transcript Abundance (nTPM)
C
Highest DC
Highest BC
p=0.0093
Degree Centrality
p=0.0063
Betweenness Centrality
p=0.0219
p=0.0227
Non-seedable
Seedable
D
DFD
Full length
Continuous
Discontinuous
CARD11
CARD19
CARD9
CASP5
CASP8
CASP9
CRADD
DEDD2
EDARADD
MALT1
MYD88
RIPK1
TRADD
AIM2
CASP1
CASP2
NLRP3
BCL10
FADD
MAVS
ASC
Sensor
Adaptor
Effector
F
PIDD1
CRADD
CASP2
EDAR
EDARADD
TRAF6
APAF1
CASP9
E
FAS
TNFRSF1A
TNFRSF10A
TNFRSF10B
RIPK1
FADD
TRADD
CASP10
CASP8
AIM2
NLRP1
MEFV
NLRP3
NLRC4
ASC
CASP1
CARD9
CARD10
CARD11
BCL10
MALT1
IFIH1
RIGI
MAVS
TRAFs

Figure 3

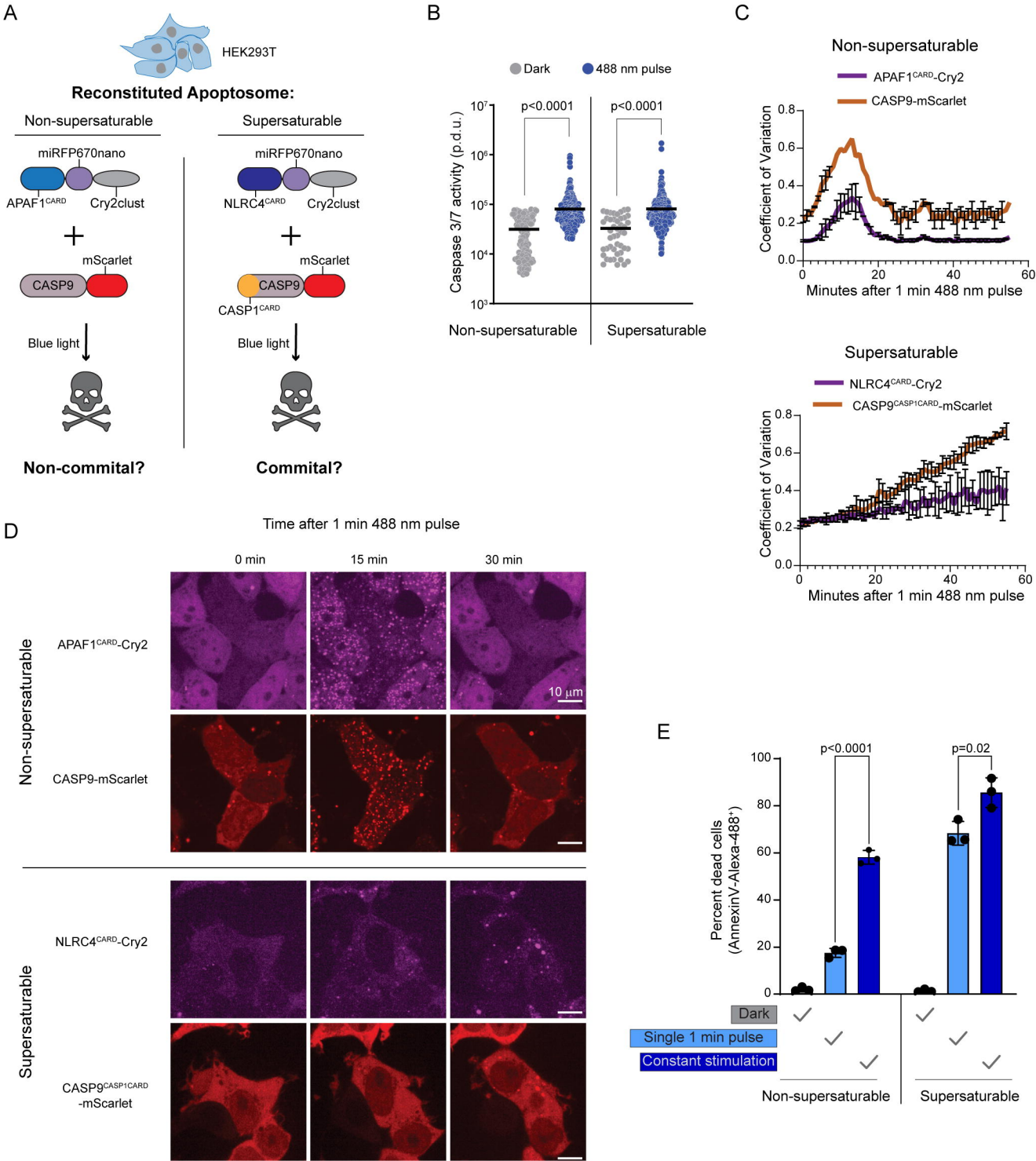
A
HEK293T
Reconstituted Apoptosome:
Non-supersaturable
Supersaturable
miRFP670nano
APAF1CARD
Cry2clust
NLRC4CARD
mScarlet
CASP9
CASP1CARD
Blue light
Non-commital?
Commital?
B
Dark
488 nm pulse
p<0.0001
p<0.0001
Caspase 3/7 activity (p.d.u.)
Non-supersaturable
Supersaturable
C
Non-supersaturable
APAF1CARD-Cry2
CASP9-mScarlet
Coefficient of Variation
Minutes after 1 min 488 nm pulse
Supersaturable
NLRC4CARD-Cry2
CASP9CASP1CARD-mScarlet
D
Time after 1 min 488 nm pulse
0 min
15 min
30 min
Non-supersaturable
APAF1CARD-Cry2
CASP9-mScarlet
10 µm
Supersaturable
NLRC4CARD-Cry2
CASP9CASP1CARD
-mScarlet
E
p<0.0001
p=0.02
Percent dead cells
(AnnexinV-Alexa-488+)
Dark
Single 1 min pulse
Constant stimulation
Non-supersaturable
Supersaturable

Figure 4

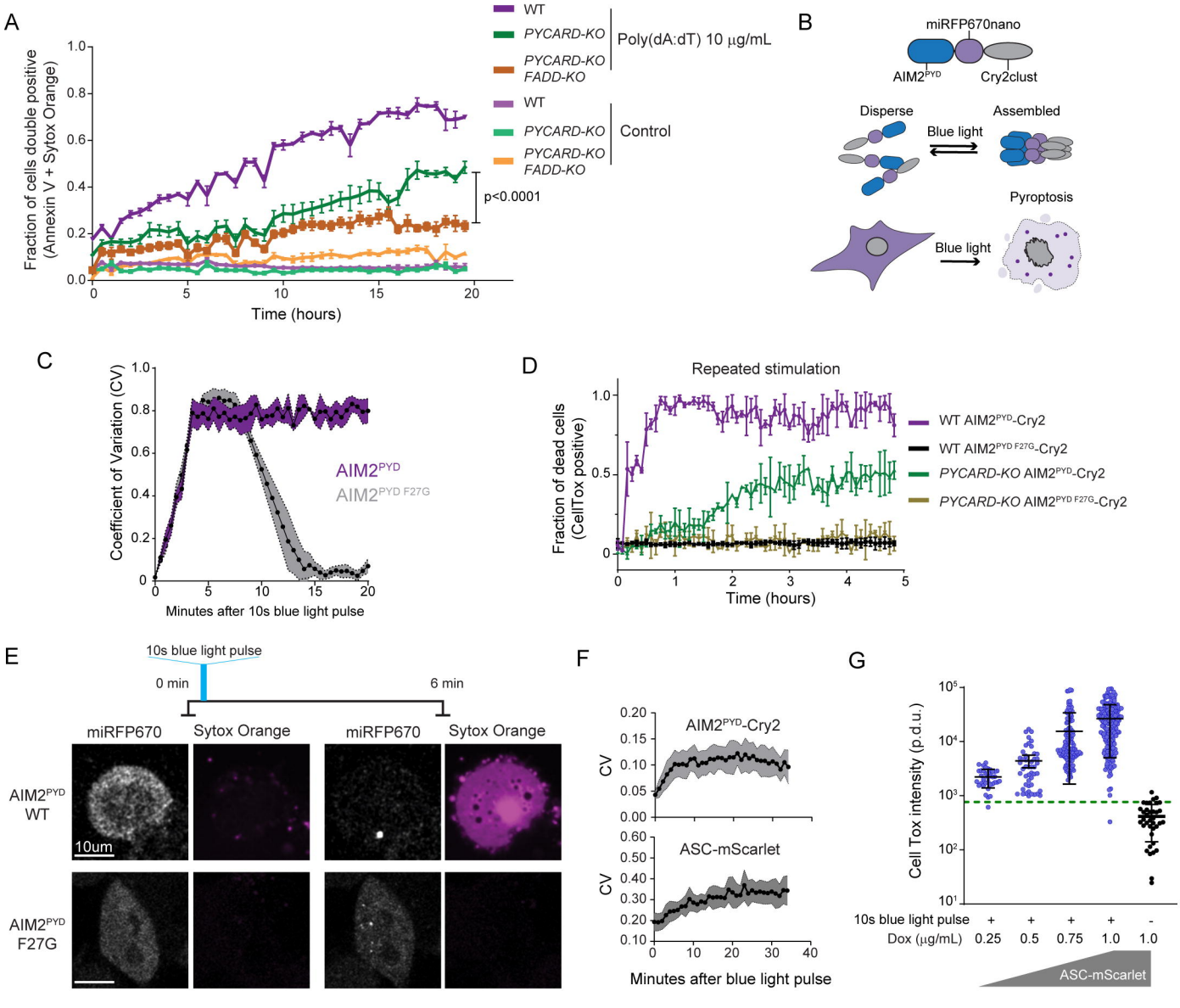
A
Fraction of cells double positive (Annexin V + Sytox Orange)
Time (hours)
WT
PYCARD-KO
PYCARD-KO FADD-KO
Poly(dA:dT) 10 μg/mL
WT
PYCARD-KO
PYCARD-KO FADD-KO
Control
p<0.0001
B
miRFP670nano
AIM2PYD
Cry2clust
Disperse
Assembled
Blue light
Pyroptosis
Blue light
C
Coefficient of Variation (CV)
Minutes after 10s blue light pulse
AIM2PYD
AIM2PYD F27G
D
Repeated stimulation
Fraction of dead cells (CellTox positive)
Time (hours)
WT AIM2PYD-Cry2
WT AIM2PYD F27G-Cry2
PYCARD-KO AIM2PYD-Cry2
PYCARD-KO AIM2PYD F27G-Cry2
E
10s blue light pulse
0 min
6 min
miRFP670
Sytox Orange
miRFP670
Sytox Orange
AIM2PYD WT
AIM2PYD F27G
10um
F
AIM2PYD-Cry2
CV
ASC-mScarlet
CV
Minutes after blue light pulse
G
Cell Tox intensity (p.d.u.)
10s blue light pulse
Dox (μg/mL)
0.25
0.5
0.75
1.0
1.0
ASC-mScarlet

Figure 5

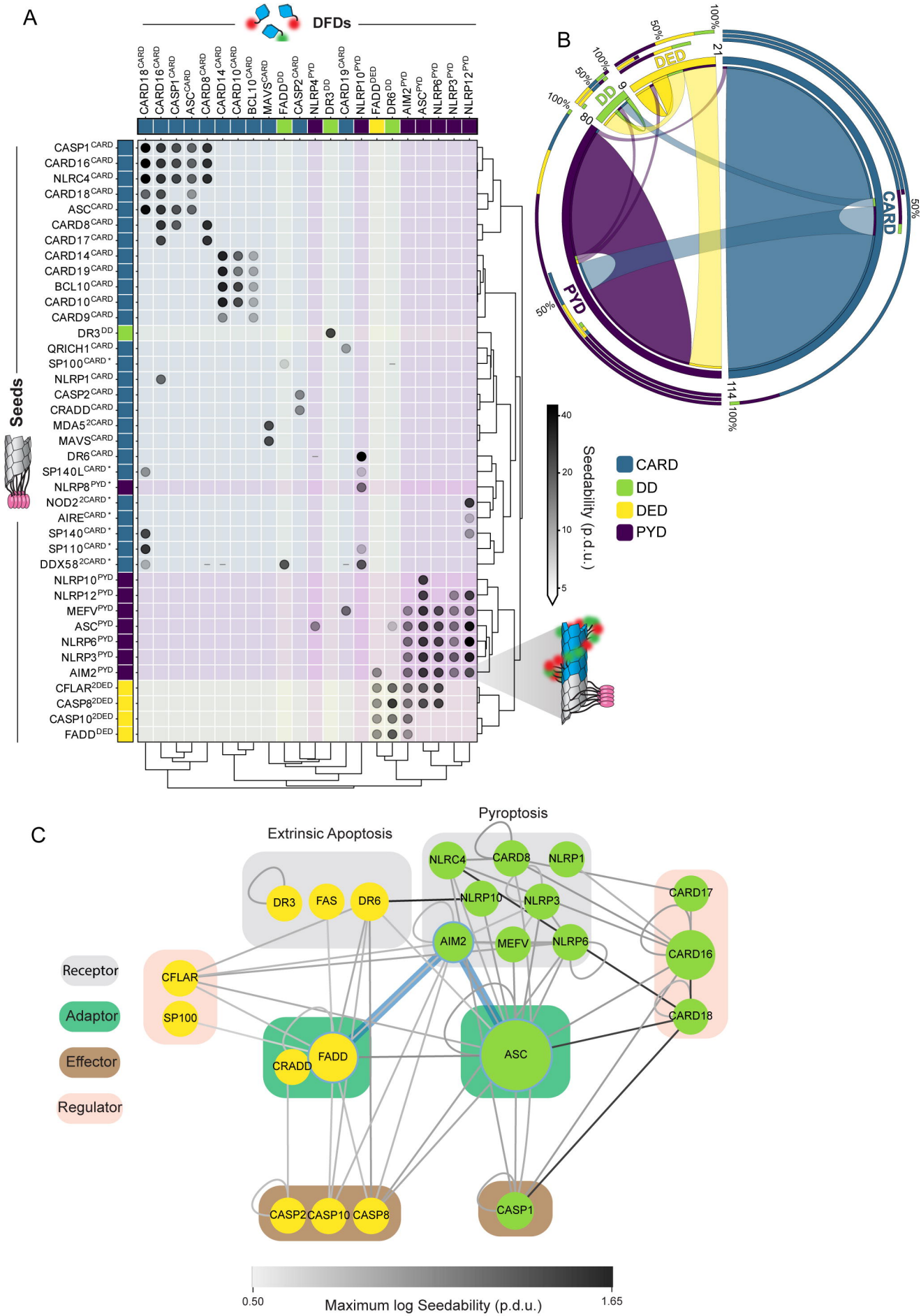
A
DFDs
Seeds
B
CARD
DD
DED
PYD
Seedability (p.d.u.)
C
Extrinsic Apoptosis
Pyroptosis
Receptor
Adaptor
Effector
Regulator
NLRC4
CARD8
NLRP1
DR3
FAS
DR6
NLRP10
NLRP3
CARD17
AIM2
MEFV
NLRP6
CARD16
CFLAR
SP100
CARD18
CRADD
FADD
ASC
CASP2
CASP10
CASP8
CASP1
0.50
Maximum log Seedability (p.d.u.)
1.65

# Figure 6

A

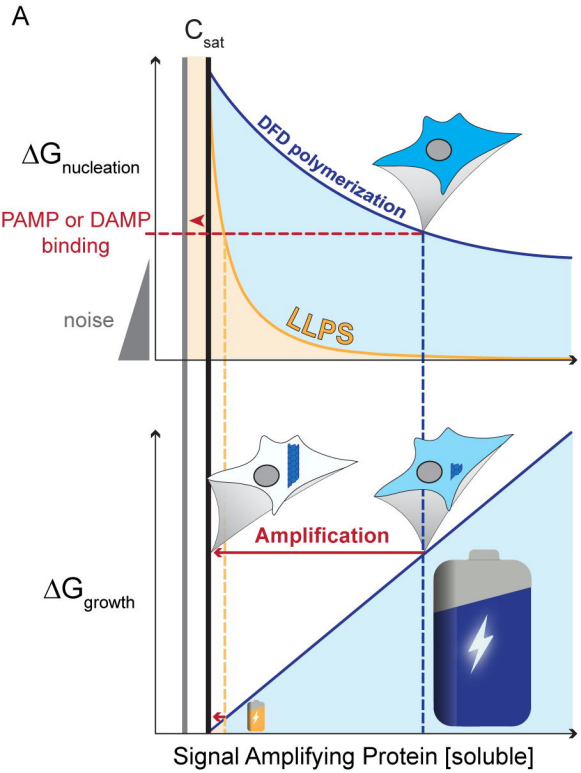
$C_{sat}$
$\Delta G_{nucleation}$
DFD polymerization
PAMP or DAMP binding
noise
LLPS
Amplification
$\Delta G_{growth}$
Signal Amplifying Protein [soluble]

B

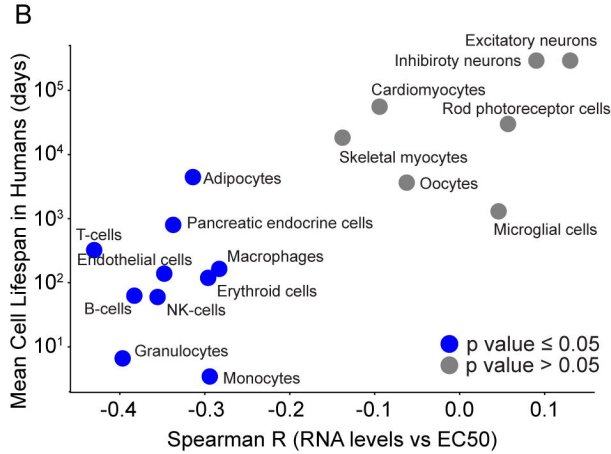
Mean Cell Lifespan in Humans (days)
$10^5$
$10^4$
$10^3$
$10^2$
$10^1$
Excitatory neurons
Inhibiroty neurons
Cardiomyocytes
Rod photoreceptor cells
Skeletal myocytes
Oocytes
Adipocytes
Microglial cells
Pancreatic endocrine cells
T-cells
Endothelial cells
Macrophages
Erythroid cells
B-cells
NK-cells
Granulocytes
Monocytes
p value ≤ 0.05
p value > 0.05
-0.4
-0.3
-0.2
-0.1
0.0
0.1
Spearman R (RNA levels vs EC50)

Figure S1

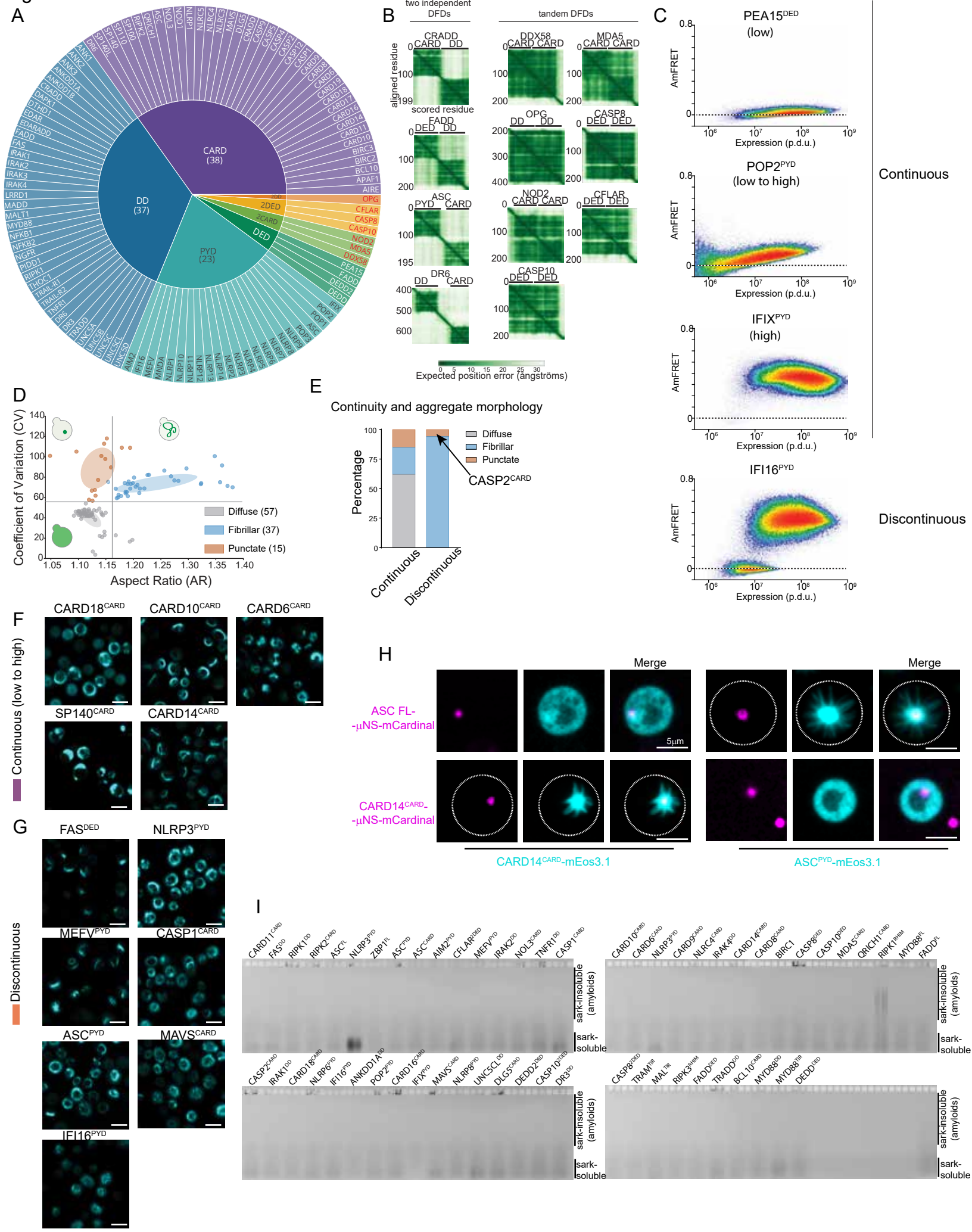
A
CARD (38)
DD (37)
PYD (23)
DED
2DED
3CARD
B
two independent DFDs
tandem DFDs
CRADD CARD DD
DDX58 CARD CARD
MDA5 CARD CARD
FADD DED DD
OPG DD DD
CASP8 DED DED
ASC PYD CARD
NOD2 CARD CARD
CFLAR DED DED
DR6 DD CARD
CASP10 DED DED
aligned residue
scored residue
Expected position error (ångströms)
C
PEA15DED (low)
POP2PYD (low to high)
IFIXPYD (high)
IFI16PYD
AmFRET
Expression (p.d.u.)
Continuous
Discontinuous
D
Coefficient of Variation (CV)
Aspect Ratio (AR)
Diffuse (57)
Fibrillar (37)
Punctate (15)
E
Continuity and aggregate morphology
Percentage
Diffuse
Fibrillar
Punctate
CASP2CARD
Continuous
Discontinuous
F
Continuous (low to high)
CARD18CARD
CARD10CARD
CARD6CARD
SP140CARD
CARD14CARD
G
Discontinuous
FASDED
NLRP3PYD
MEFVPYD
CASP1CARD
ASCPYD
MAVSCARD
IFI16PYD
H
Merge
ASC FL-µNS-mCardinal
CARD14CARD-µNS-mCardinal
5µm
CARD14CARD-mEos3.1
ASCPYD-mEos3.1
I
sark-insoluble (amyloids)
sark-soluble

Figure S2

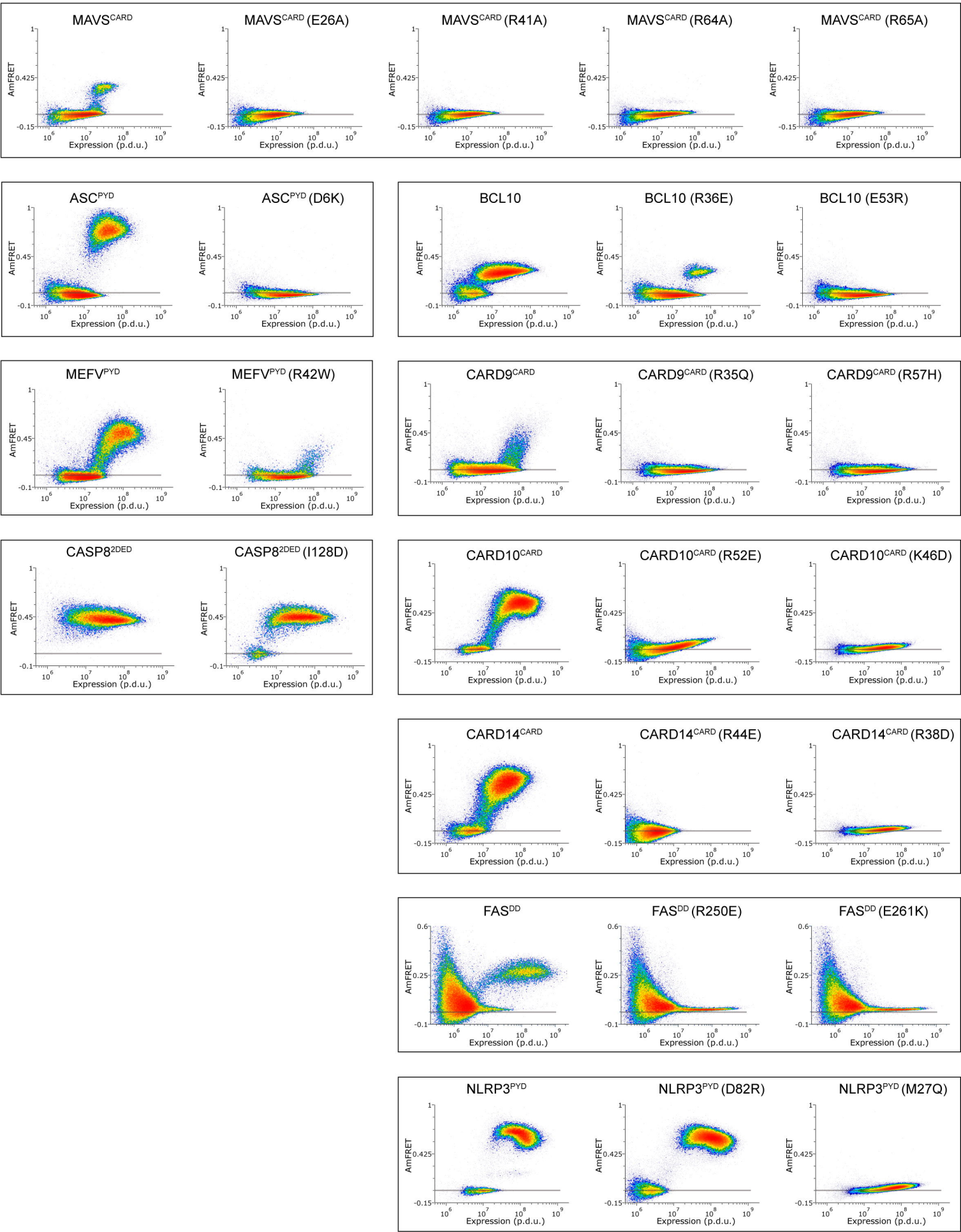
MAVS^CARD
MAVS^CARD (E26A)
MAVS^CARD (R41A)
MAVS^CARD (R64A)
MAVS^CARD (R65A)
ASC^PYD
ASC^PYD (D6K)
BCL10
BCL10 (R36E)
BCL10 (E53R)
MEFV^PYD
MEFV^PYD (R42W)
CARD9^CARD
CARD9^CARD (R35Q)
CARD9^CARD (R57H)
CASP8^2DED
CASP8^2DED (I128D)
CARD10^CARD
CARD10^CARD (R52E)
CARD10^CARD (K46D)
CARD14^CARD
CARD14^CARD (R44E)
CARD14^CARD (R38D)
FAS^DD
FAS^DD (R250E)
FAS^DD (E261K)
NLRP3^PYD
NLRP3^PYD (D82R)
NLRP3^PYD (M27Q)
AmFRET
Expression (p.d.u.)

Figure S3

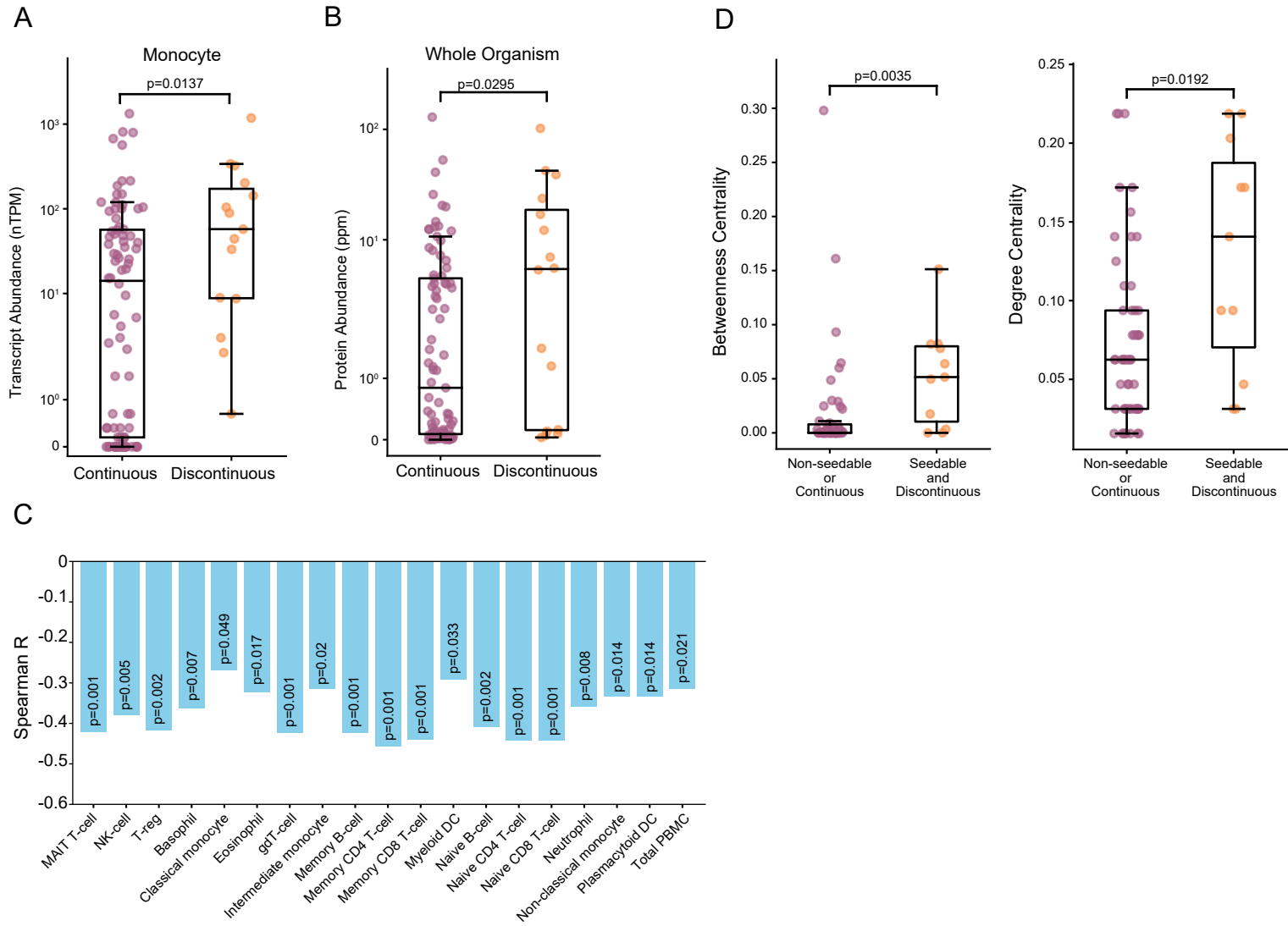
A
Monocyte
p=0.0137
Transcript Abundance (nTPM)
Continuous
Discontinuous
B
Whole Organism
p=0.0295
Protein Abundance (ppm)
Continuous
Discontinuous
D
p=0.0035
Betweenness Centrality
Non-seedable or Continuous
Seedable and Discontinuous
p=0.0192
Degree Centrality
Non-seedable or Continuous
Seedable and Discontinuous
C
Spearman R
p=0.001
p=0.005
p=0.002
p=0.007
p=0.049
p=0.017
p=0.001
p=0.02
p=0.001
p=0.001
p=0.001
p=0.033
p=0.002
p=0.001
p=0.001
p=0.008
p=0.014
p=0.014
p=0.021
MAIT T-cell
NK-cell
T-reg
Basophil
Classical monocyte
Eosinophil
gdT-cell
Intermediate monocyte
Memory B-cell
Memory CD4 T-cell
Memory CD8 T-cell
Myeloid DC
Naive B-cell
Naive CD4 T-cell
Naive CD8 T-cell
Neutrophil
Non-classical monocyte
Plasmacytoid DC
Total PBMC

Figure S4

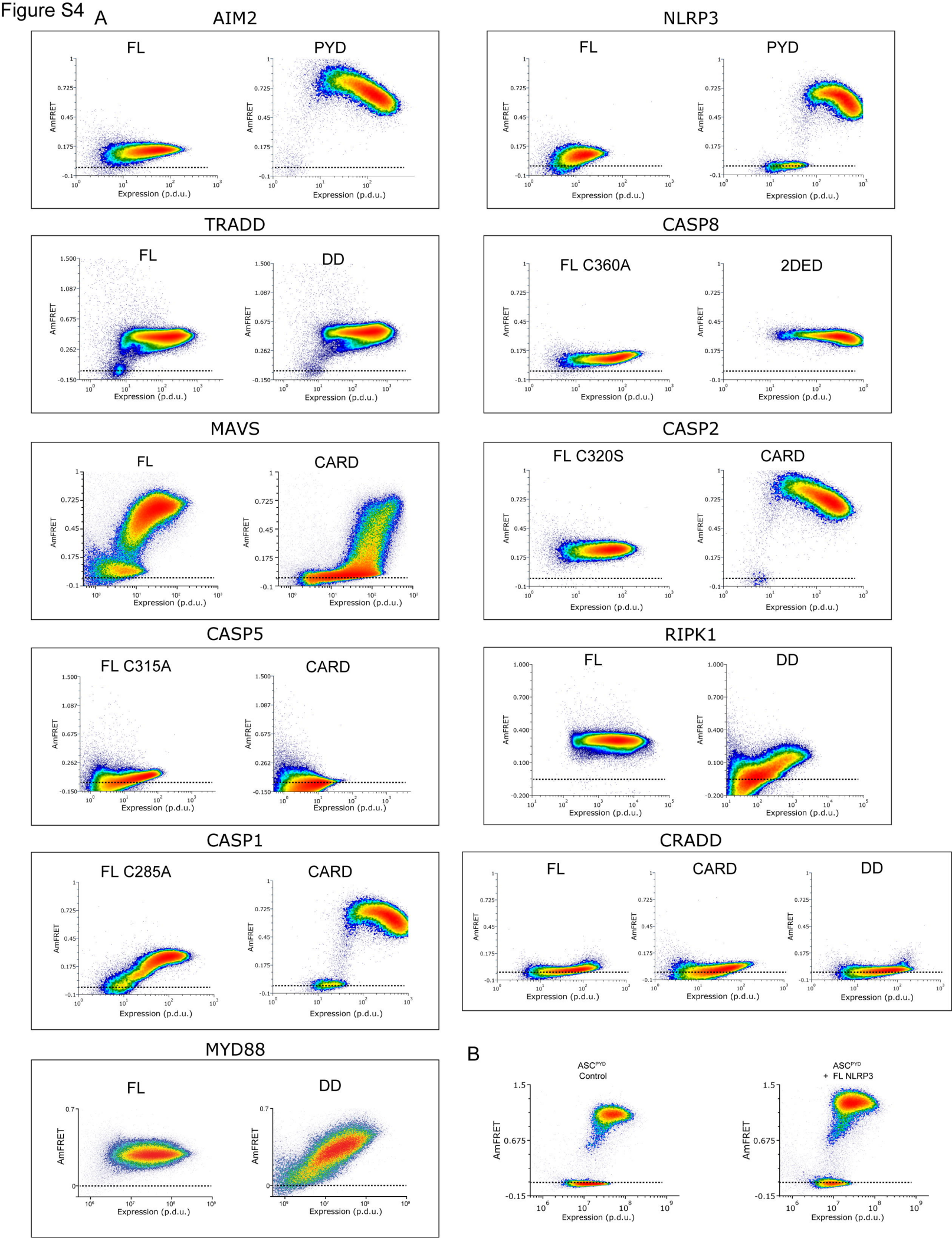
A
AIM2
FL
PYD
NLRP3
FL
PYD
TRADD
FL
DD
CASP8
FL C360A
2DED
MAVS
FL
CARD
CASP2
FL C320S
CARD
CASP5
FL C315A
CARD
RIPK1
FL
DD
CASP1
FL C285A
CARD
CRADD
FL
CARD
DD
MYD88
FL
DD
B
ASC^PYD
Control
ASC^PYD
+ FL NLRP3
AmFRET
Expression (p.d.u.)

Figure S5

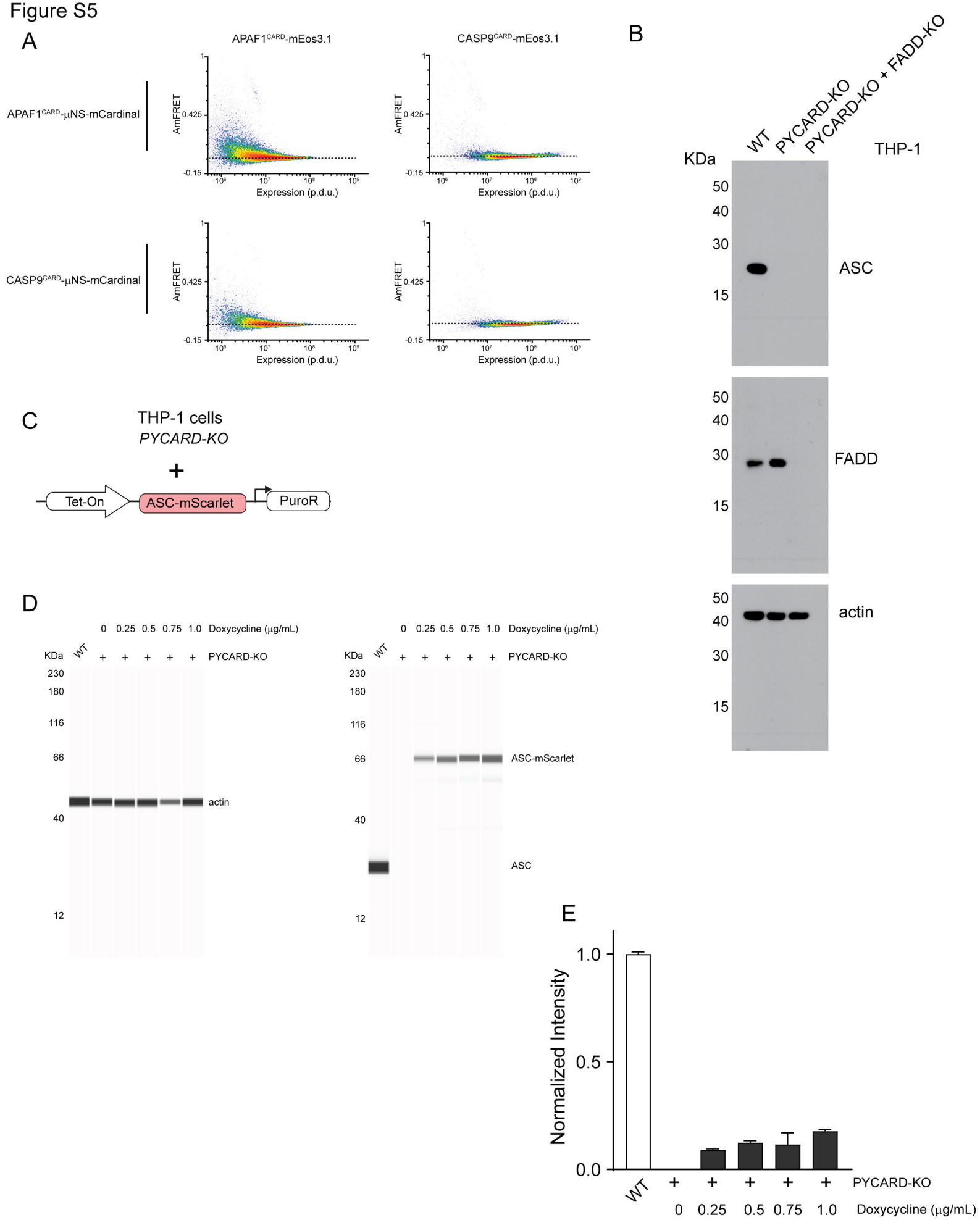
A
APAF1CARD-mEos3.1
CASP9CARD-mEos3.1
APAF1CARD-μNS-mCardinal
CASP9CARD-μNS-mCardinal
AmFRET
Expression (p.d.u.)
B
WT
PYCARD-KO
PYCARD-KO + FADD-KO
THP-1
KDa
ASC
FADD
actin
C
THP-1 cells
PYCARD-KO
+
Tet-On
ASC-mScarlet
PuroR
D
0 0.25 0.5 0.75 1.0 Doxycycline (μg/mL)
KDa
WT
PYCARD-KO
actin
ASC-mScarlet
ASC
E
Normalized Intensity
PYCARD-KO
Doxycycline (μg/mL)

Figure S6

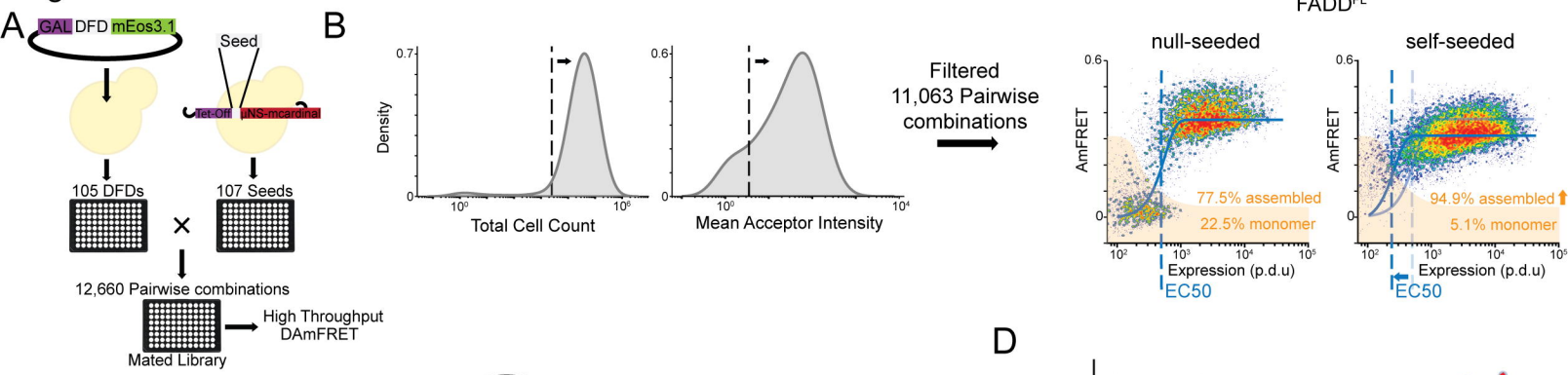


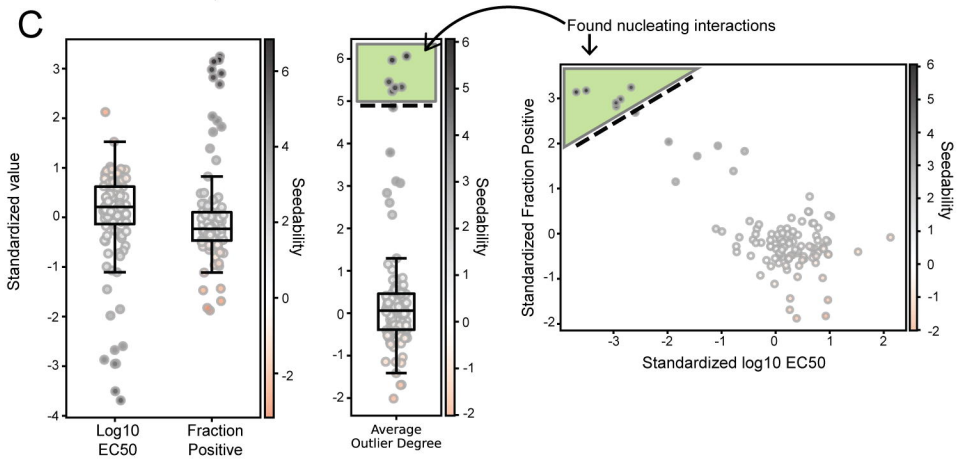


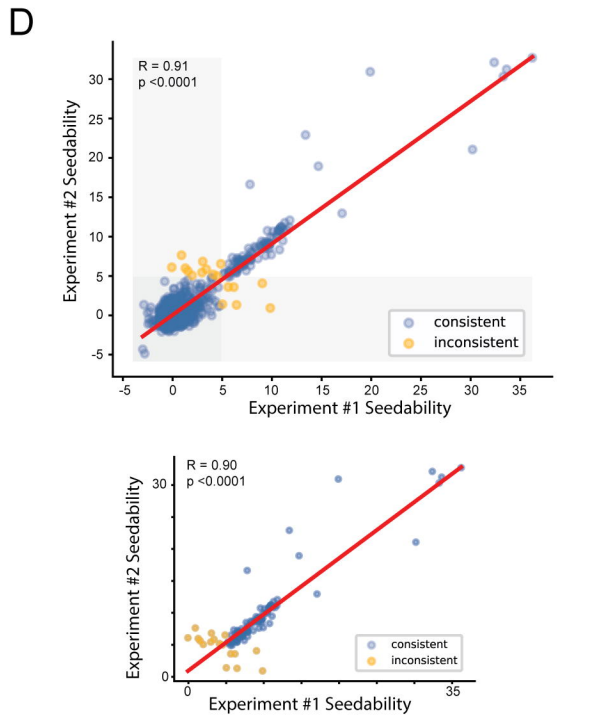


E

| DFD | seed | Experiment 1 Seedability | Experiment 2 Seedability | Experiment 1 Hit | Experiment 2 Hit |
|---|---|---|---|---|---|
| BCL10$^{CARD}$ | CARD9$^{CARD}$ | 5.605122471 | 3.593963956 | 1 | 0 |
| CARD16$^{CARD}$ | CARD18$^{CARD}$ | 9.031467777 | 4.066339437 | 1 | 0 |
| CASP1$^{CARD}$ | NLRP1$^{CARD}$ | 1.545796004 | 5.626068716 | 0 | 1 |
| CASP1$^{CARD}$ | CARD18$^{CARD}$ | 1.960096395 | 5.058239356 | 0 | 1 |
| NLRP12$^{PYD}$ | NLRP12$^{PYD}$ | 9.833643227 | 0.923192774 | 1 | 0 |
| NLRP12$^{PYD}$ | CASP8$^{2DED}$ | -0.077027772 | 6.096560096 | 0 | 1 |
| NLRP12$^{PYD}$ | MAVS$^{CARD}$ | 0.903552494 | 7.635310335 | 0 | 1 |
| NLRP4$^{PYD}$ | ASC$^{PYD}$ | 6.442627262 | 1.323929864 | 1 | 0 |
| NLRP6$^{PYD}$ | NLRP12$^{PYD}$ | 4.094918773 | 5.191326792 | 0 | 1 |
| NLRP6$^{PYD}$ | NLRP10$^{PYD}$ | 3.041813188 | 6.829209115 | 0 | 1 |
| ASC$^{CARD}$ | CARD18$^{CARD}$ | 6.168228462 | 3.5821944 | 1 | 0 |
| ASC$^{FL}$ | NLRP1$^{CARD}$ | 1.285512745 | 5.981526181 | 0 | 1 |
| ASC$^{FL}$ | CARD18$^{CARD}$ | 3.391100621 | 5.856338231 | 0 | 1 |
| ASC$^{PYD}$ | POP1$^{PYD}$ | 2.96059311 | 5.436659622 | 0 | 1 |
| DR6$^{DD}$ | AIM2$^{PYD}$ | 4.8571763 | 6.533971615 | 0 | 1 |
| DR6$^{DD}$ | NLRP6$^{PYD}$ | 4.493927648 | 4.971884105 | 0 | 1 |
| UNC5A$^{DD}$ | MAVS$^{CARD}$ | 5.021870847 | 1.407364391 | 1 | 0 |

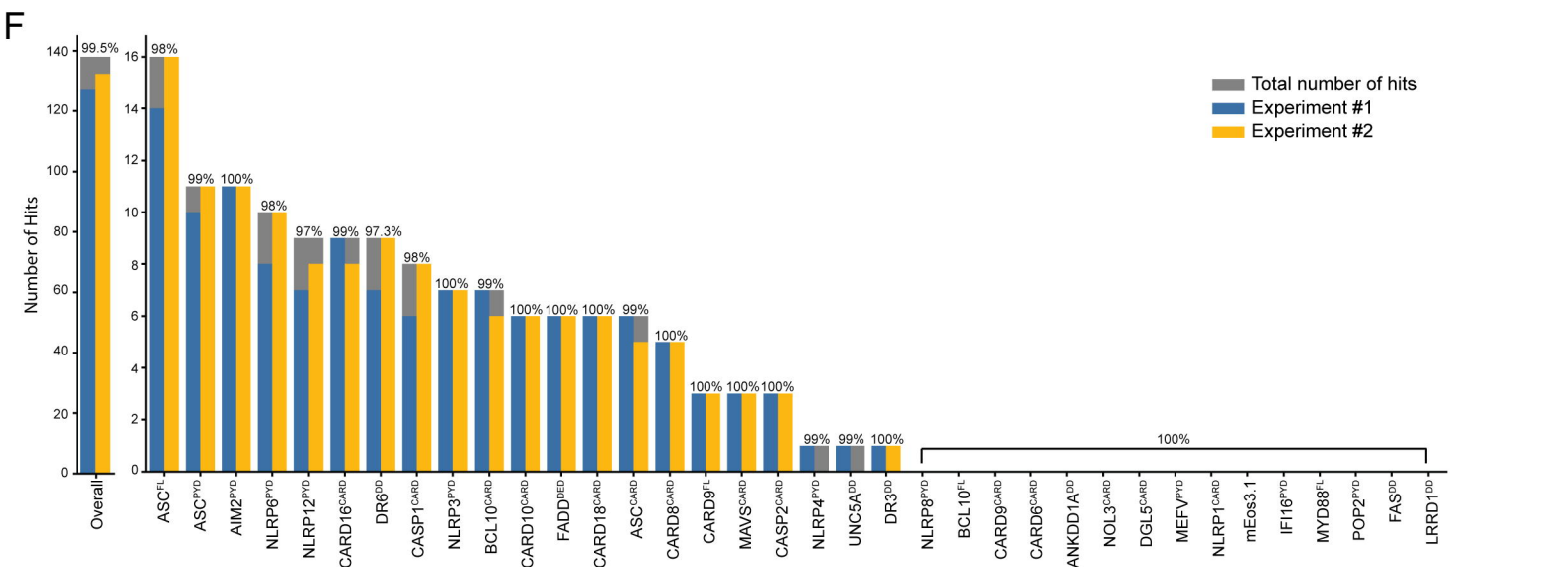

Figure S7

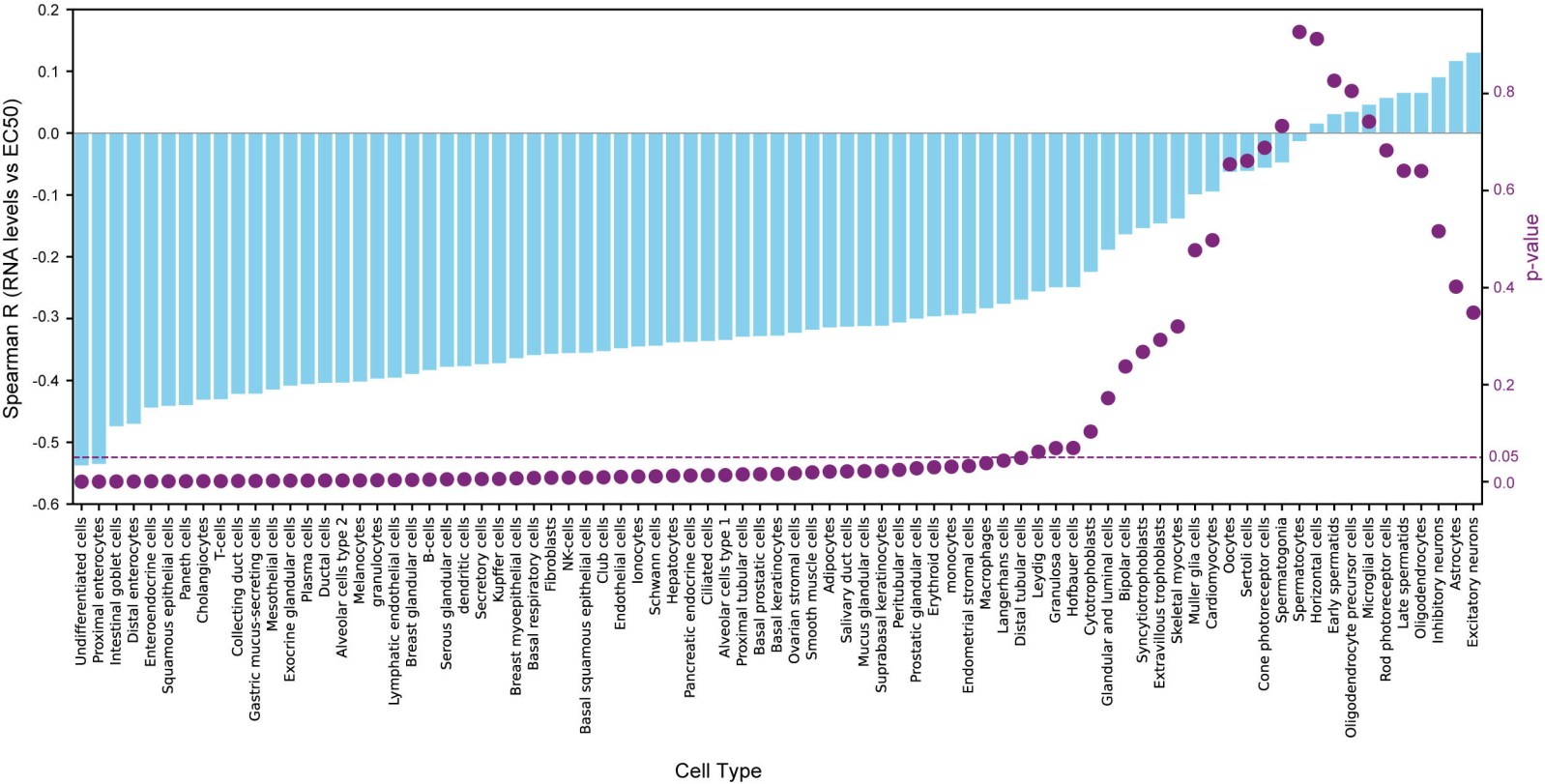
Spearman R (RNA levels vs EC50)
p-value
Cell Type
0.2
0.1
0.0
-0.1
-0.2
-0.3
-0.4
-0.5
-0.6
0.8
0.6
0.4
0.2
0.05
0.0
Undifferentiated cells
Proximal enterocytes
Intestinal goblet cells
Distal enterocytes
Enteroendocrine cells
Squamous epithelial cells
Paneth cells
Cholangiocytes
T-cells
Collecting duct cells
Gastric mucus-secreting cells
Mesothelial cells
Exocrine glandular cells
Plasma cells
Ductal cells
Alveolar cells type 2
Melanocytes
granulocytes
Lymphatic endothelial cells
Breast glandular cells
B-cells
Serous glandular cells
dendritic cells
Secretory cells
Kupffer cells
Breast myoepithelial cells
Basal respiratory cells
Fibroblasts
NK-cells
Basal squamous epithelial cells
Club cells
Endothelial cells
Ionocytes
Schwann cells
Hepatocytes
Pancreatic endocrine cells
Ciliated cells
Alveolar cells type 1
Proximal tubular cells
Basal prostatic cells
Basal keratinocytes
Ovarian stromal cells
Smooth muscle cells
Adipocytes
Salivary duct cells
Mucus glandular cells
Suprabasal keratinocytes
Peritubular cells
Prostatic glandular cells
Erythroid cells
monocytes
Endometrial stromal cells
Macrophages
Langerhans cells
Distal tubular cells
Leydig cells
Granulosa cells
Hofbauer cells
Cytotrophoblasts
Glandular and luminal cells
Bipolar cells
Syncytiotrophoblasts
Extravillous trophoblasts
Skeletal myocytes
Muller glia cells
Cardiomyocytes
Oocytes
Sertoli cells
Cone photoreceptor cells
Spermatogonia
Spermatocytes
Horizontal cells
Early spermatids
Oligodendrocyte precursor cells
Microglial cells
Rod photoreceptor cells
Late spermatids
Oligodendrocytes
Inhibitory neurons
Astrocytes
Excitatory neurons